

# The Timing Properties of Sco X-1 along its Z track with EXOSAT.

Stefan W. Dieters<sup>1</sup> and Michiel van der Klis<sup>2</sup>

<sup>1</sup>*CSPAR, University of Alabama In Huntsville, Huntsville, AL 35899, U.S.A.*

<sup>2</sup>*Astronomical Institute, "Anton Pannekoek", University of Amsterdam, Kruislaan 403, 1098 SJ Amsterdam, The Netherlands*

## Abstract.

We present a systematic, homogeneous analysis of all the EXOSAT ME, high time resolution data on Sco X-1. We investigate, for the first time, all power spectral properties of the  $<100$  Hz quasi-periodic oscillations (QPO) and noise of Sco X-1 as a function of position on the Z-shaped track traced out in the X-ray colour-colour diagram. For this purpose, we introduce a new generally applicable method for parametrizing the position of a source on its track in a colour-colour or hardness-intensity diagram. Generally, the properties of Sco X-1 vary smoothly as a function of position along the Z track. However, some variability parameters change abruptly at either of the vertices of the Z track indicating that the branches of the Z track represent distinct source states not only in spectral state but also in rapid variability characteristics. All variability components are found to have energy spectra harder than the average flux. We show that the very low frequency noise (VLFN) is consistent with being solely due to motion along the Z track. The power spectra of the X-ray intensity as well as source position along the Z track extend, unbroken, to time scales of nearly 1 day. We study the high frequency noise (HFN) component for the first time in sufficient detail to show that there are changes in the HFN cut-off frequency with position on the Z track. It changes abruptly from  $\sim 75$  Hz to  $\sim 35$  Hz at the normal/flaring branch vertex. The HFN is found to extend out to about 300 Hz. The QPO show a remarkably rapid change in frequency at or just before the normal-branch/flaring-branch (NB/FB) vertex. This transition happens within 1.5% of the entire extent of the Z track. The QPO themselves are visible for 17% of the Z. We find a new sort of behaviour near the NB/FB vertex, i.e., rapid excursions from the NB into the FB and back again taking only a few minutes. We found several indications that position on the Z track is not the only parameter governing the behaviour of Sco X-1. The most dramatic examples of this are two brief episodes where the QPO frequency changed rapidly without the usual changes in colours and intensity which accompany a change of source state. In one case the frequency rapidly rose from 6 Hz to 16 Hz, and then returned to 6 Hz, while Sco X-1 apparently remained unmoved on the normal branch in the colour-colour diagram. In the second case the QPO frequency changed from 16 Hz to 7 Hz without the usual indications of a passage through the normal/flaring branch vertex (simultaneous dips in the count rate and colours as the frequency changes through 8 Hz). Thus it seems that deviations from the usual one to one correspondence between QPO behaviour and spectral state, perhaps due to QPO frequency mode switching do occasionally occur.

## Keywords.

accretion, accretion disks—instrumentation: detectors—binaries: close  
—stars: individual: Sco X-1—stars: neutron: Z-sources—X-rays: stars

## Thesaurus Codes.

02.01.2—03.09.1—08.02.1—08.09.2:Sco X-1—08.14.1:Z-sources—13.25.5

## 1: Introduction.

Sco X-1 is a low mass X-ray binary (LMXB). These systems consist of a neutron star or a black hole and an accretion disk fed by Roche lobe overflow from a low mass ( $\leq 2 M_{\odot}$ ) companion. The optical and X-ray fluxes of LMXBs are dominated by processes in or near the accretion disk. Persistently bright LMXBs such as Sco X-1 are thought to contain a neutron star, because two similar systems show type I bursts (i.e., GX 17+2; Sztajno *et al.* 1986, Kuulkers *et al.* 1997 and Cyg X-2; Kuulkers *et al.* 1995). In the cases of Sco X-1 and Cyg X-2 the companions must be

evolved, as the orbital periods are long (19.2 hr and 252 hr, respectively) and the inferred mass accretion rates are high. No X-ray pulsations have been detected from any of the persistently bright LMXBs (Vaughan *et al.* 1994).

Since its discovery (Giacconi *et al.* 1962) Sco X-1 has been extensively observed in many different wavelength bands (e.g., correlated optical/X-ray photometry: Mook *et al.* 1975, Petro *et al.* 1981, Augusteijn *et al.* 1992, McNamara *et al.* 1994, optical spectroscopy: La Sala and Thorstensen 1985, radio: Hjellming *et al.* 1990, UV: Vrtilik *et al.* 1990, 1991, hard X-rays: Jain *et al.* 1984, Ubertini *et al.* 1992). The discovery (van der Klis *et al.* 1985, Hasinger *et al.* 1986, Middleditch & Priedhorsky 1986) of rapid ( $\sim 15\text{--}55\text{ Hz}$ ) and slow ( $\sim 6\text{ Hz}$ ) quasi periodic oscillations (QPO) in the X-ray flux of the brightest LMXBs opened a way to a greater understanding of the accretion flow close to the compact object in these systems. Observations show that the properties of the QPO and associated noise components are related to the source's spectral state. The spectral state is most easily determined by using an X-ray colour-colour diagram (CD). On such a diagram six of the brightest LMXBs trace out a distorted Z shaped path; they are therefore called 'Z' sources. These sources are GX 5-1, Cyg X-2, GX 340+0, GX 349+2, GX 17+2, and Sco X-1.

The three branches of the Z are called the horizontal branch (HB: topmost stroke), the normal branch (NB: the downward stroke) and the flaring branch (FB: the bottom stroke). The branch names are mostly historical; the horizontal branch is not necessarily horizontal, the source may or may not spend most of its time in the normal branch, and only Sco X-1, GX 17+2 (Penninx *et al.* 1990) and GX 349+2 (Ponman *et al.* 1988) show flares in the flaring branch. The normal and flaring branches of Sco X-1 correspond to the well documented (e.g., Mook *et al.* 1975, Petro *et al.* 1981 and Hertz *et al.* 1992) quiescent and active states seen at both optical and X-ray wavelengths (Augusteijn *et al.* 1992, Hasinger 1987a, Priedhorsky *et al.* 1986).

There are six distinguishable components in the power spectra of Z sources (e.g. van der Klis 1989a, 1995a,b). The very low frequency noise (VLFN) is well fitted by a power law. It dominates the power spectrum below 0.1 Hz. High frequency noise (HFN) is approximately flat out to a frequency near 50-100 Hz and then slopes down towards higher frequencies. It has been fitted with either an exponentially cut-off power law or a Lorentzian peak centered at zero frequency. The low frequency noise (LFN) either appears as a component that is decreasing monotonically with frequency ("red noise") and extends out to about 10 Hz; or in other sources it has the shape of a very broad peak with a central frequency near 2 Hz. It has been represented by an exponentially cut-off power law (red or peaked depending on the sign of the power law index), or by a Lorentzian peak centered at zero frequency (red), or near 2 Hz (peaked). Finally, there are three distinct types of QPO; one associated with the horizontal branch with frequencies between 5 and 55 Hz, another associated with the normal and flaring branches (6-20 Hz) and a pair of kHz frequency QPO (see van der Klis 1998 for a review of kHz QPO). This paper deals with the first two mentioned types of QPO only. These QPO have been fitted by Lorentzian or Gaussian peaks.

Both the VLFN and the HFN are observed in all branches. The LFN is observed only in the horizontal branch, and in the very upper part of the normal branch. Also observed in this part of the Z track are intensity dependent  $\sim 15\text{--}55\text{ Hz}$  QPO, the horizontal branch QPO (HBO). When HBO are observed, LFN is always present as well. On the mid- to lower NB another distinct type of QPO is observed. Occasionally these normal branch oscillations (NBO) occur simultaneously with the HBO. The NBO frequency remains approximately constant at a frequency near 6 Hz despite 30% changes in intensity when the source moves up and down the normal branch. In Sco X-1 (Priedhorsky *et al.* 1986) it has been observed that when the source moves into the lower part of the FB, the QPO frequency increases from 6 Hz to at most  $\sim 21\text{ Hz}$ . Further up the FB the QPO melt into a continuum of HFN. These high frequency QPO are called flaring branch oscillations (FBO). They have also been seen in GX 17+2 (Penninx *et al.* 1990, Kuulkers *et al.* 1997). The FBO are thought to be closely related to the NBO because of the continuous transition from one to the other (the QPO found in the flaring branch of Cyg X-2, Kuulkers & van der Klis 1995, may be another phenomenon). The properties of the various power spectral components are summarized in Table 1 of van der Klis (1989a) and Fig. 1 of Lamb (1989). See also the reviews of Lewin, van Paradijs, and van der Klis (1988) and van der Klis (1989a,b, 1995a,b, 1998).

The tight correlation of all observables with the instantaneous position of the source on the Z-track

and the continuous nature of the motion along the Z track suggest that there is only one underlying physical parameter responsible. The obvious candidate is the mass accretion rate,  $\dot{M}$ . In Sco X-1 and Cyg X-2 it is observed that the ultraviolet-line and -continuum fluxes (Vrtilek *et al.* 1990,1991, Hasinger *et al.* 1990) and the optical brightness (Augusteijn *et al.* 1992) all increase as the source moves from the left-most end of the horizontal branch along the Z track toward and up the flaring branch. This indicates that  $\dot{M}$  increases along the Z track in this sense (Hasinger *et al.* 1990). The NB/FB transition is thought to occur near the Eddington limit (Lamb 1989). Note that the X-ray count rate is not a good measure of  $\dot{M}$  as it increases in both directions away from the NB/FB vertex, up the NB as well as up the FB.

Different models have been proposed for the HBO and the NBO/FBO. The most successful explanation for the HBO is given by the “beat-frequency model” of Alpar and Shaham (1985; also Lamb *et al.* 1985). Here matter is quasi-periodically removed by the neutron stars’ magnetic field from the inner edge of the accretion disk. According to the model of Fortner *et al.* (1989) for the the NBO/FBO, these oscillations originate in a cool radial inflow surrounding the neutron star and its magnetosphere. This region is prominent only at luminosities near the Eddington luminosity ( $L_{Edd}$ ) when, as already pointed out by Hasinger (1987a), radiation force significantly slows the in-falling material. Under these circumstances opacity-driven instabilities can develop with properties consistent with those observed in the NBO. According to Lamb (1989), near  $L_{Edd}$  the flow becomes unstable and photo-hydrodynamic oscillations are excited with frequencies ranging from near 6 Hz to greater than 10 Hz, as seen in moving from the NB to the FB. A different model for NBO/FBO, where these oscillations are caused by sound waves in a thick, torus-like inner accretion disk, has been proposed by Alpar *et al.* (1992).

Compared to Cyg X-2 and GX 5-1, the sources Sco X-1 and GX 17+2 have short horizontal branches which are oriented nearly vertically. No HBO were detected using EXOSAT on the HB of Sco X-1 (which itself was observed only once; Hasinger, Priedhorsky and Middleditch 1989, hereafter HPM89). However van der Klis *et al.* (1997) report, using RXTE observations, a QPO feature with properties similar to HBO in Sco X-1. The LFN of Sco X-1 and GX 17+2 (Langmeier *et al.* 1990, Penninx *et al.* 1990, Kuulkers *et al.* 1997) has a peak near 2 Hz, whereas in Cyg X-2, GX 5-1 and GX 340+0 it has a “red” (monotonically decreasing with frequency) shape. Sco X-1, GX 17+2 and GX 349+2 have prominent flaring branches with classic flaring behaviour, while GX 5-1 and Cyg X-2 have small FBs. In these two sources, the count rate dips, rather than flaring, when the source moves into the FB. GX 340+0 also has a weak FB, with a combination of both dipping and flaring behaviour (Penninx *et al.* 1991, Kuulkers & van der Klis 1996). While FBO have been observed from Sco X-1, and GX 17+2, they are weak for GX 340+0 (Penninx *et al.* 1991, Kuulkers & van der Klis, 1996), or absent on the flaring branches of GX 5-1 (Kuulkers *et al.* 1994). These systematic differences suggest that there are two types of Z source, or that Sco X-1 and Cyg X-2 are near the two extremes of a continuous range of behaviour differences, possibly governed by inclination angle (Hasinger & van der Klis 1989, Kuulkers *et al.* 1994, 1997), or neutron star magnetic field strength (Psaltis, Lamb & Miller, 1995).

Most of the observational material gathered with EXOSAT on Sco X-1 has been previously analysed (Middleditch & Priedhorsky 1986, Priedhorsky *et al.* 1986, Pollock *et al.* 1986, van der Klis *et al.* 1987, HPM89). Ginga data on Sco X-1 were reported by Hertz *et al.* (1992). These studies concentrated upon individual observations and hence were necessarily fragmentary and without the benefit of our current more global view of Z source behaviour. Here, we present the first comprehensive and homogeneous analysis of the EXOSAT Sco X-1 data. As part of a project to look for rapid power fluctuations, we examine these data in much greater detail than in previous studies. Particular attention is paid to freezing any changes in QPO properties associated with changes in brightness or position upon the colour-colour diagram. We introduce a new method for parametrizing the position along the Z track, which can be applied to colour-colour tracks of any shape. We study the variation of all power spectral components as a function of position along the Z track for all branches in a consistent manner. The behaviour of the QPO near the NB/FB vertex is closely examined, and three different types of behaviour are identified. A previously unrecognized, rapid form of the NB/FB transition is noted. Near the NB/FB transition, the QPO frequency is found to be very sensitive to position along the Z track: the change from 7.5 Hz to 12 Hz occurs within 1.5% of the span of the Z track. We present two cases where Sco X-1 seemed not to follow usual Z-source behaviour of smooth motion along the Z track with strictly correlated

changes in fast variability properties.

## 2: Observations and Analysis.

Sco X-1 was observed several times with the EXOSAT satellite during the period 1983 to 1986. We used data taken with the medium energy (ME) instrument (Turner, Smith and Zimmermann 1981, White and Peacock 1988). The array of 8 ME detectors was arranged in two half arrays of 4 detectors, i.e., half 1: detectors 1–4 and half 2: detectors 5–8. Each detector consisted on an argon filled proportional counter atop a xenon filled proportional counter separated by a thin mylar window. The Ar counters were sensitive over the 1 to 20 keV range while the Xe counters were sensitive over the 5 to 50 keV range. There were 4 thick (numbers 1,2,5,6) and 4 thin (3,4,7,8) windowed Ar detectors; these had substantially different energy responses. Each counter could be individually switched on or off. Each half array of detectors could be pointed in slightly different directions. The On Board Computer (OBC) could be programmed to collect, simultaneously, data in several modes. These modes were separated into High Time Resolution (HTR) and High Energy Resolution (HER) modes. We examined all observations, but we concentrated on observations where energy resolved data and high time resolution data were simultaneously available. An observation log is shown in Table 1. The background in the Xe counters was always near 75 cts/sec/counter while the Ar background was much lower, about 12 cts/sec/counter. We did not use the early 1983 observations because of the many detector set-up changes and the low time resolutions used in both the HER and HTR modes.

The most common set-up used for observing Sco X-1 was with one half array with only the argon counters switched on, and the other half array with only the xenon counters switched on. The Xe half (array half 2) was in all observations pointed directly at Sco X-1 while the Ar half (array half 1) was usually offset to a collimator response of 8–12%. This was done to avoid damage to the Ar counters from high count rates. Generally the argon counters were used to collect data in 4 energy channels at time resolutions between 4 and 16 ms (HER7 mode, I7 data) while the xenon counters were used to produce data in one energy channel with a 1 or 2 ms time resolution (HTR3 or HTR5, T3 or T5 data). The setup was different on Feb 25, 1985, when data were collected from all eight Xe counters, which were pointed directly at Sco X-1, but no Ar data were collected. Another exceptional observation (3 Aug 1984) had all 8 (Ar+Xe) detectors on and used a higher collimator response than usual (12–23% rather than 8–12%). During this observation the OBC was programmed to give the combined Ar+Xe detector count rate every 8 ms (HTR3, T3 data) and Ar and Xe multichannel energy data every 32 ms (HER5 mode, E5 data). The resulting count rates were  $\sim 5900$  cts/sec in the NB, reaching a maximum of 9800 cts/sec in the FB. The peak count rate is the highest recorded in any EXOSAT observation.

The energy boundaries of the four I7 channels normally used were 0.9, 3.1, 4.9, 6.6 and 19.5 keV. The four Ar bands defined by these boundaries we will call bands 1 to 4, respectively. We converted the Aug 1984 E5 data into 4 channel data with the same energy boundaries as the I7 data.

When we report Xe count rates the numbers will always refer to background corrected count rates over the full Xe energy range and reduced to counts per whole array (8 detectors) at 100% collimator response. The deadtime corrections for the Xe HTR mode data were small ( $<1\%$ ) and here will provide a valuable framework in which to assess more recent RXTE observations. The Ar count rates are background and deadtime corrected (Andrews & Stella 1985) and scaled to a 10% collimator response for 8 detectors. Although the latest collimator response calibration (Kuulkers *et al.* 1994, Kuulkers 1995) was used, the collimator responses at the large offsets used for Sco X-1 with the Ar detectors are somewhat uncertain. The systematic uncertainty in the corrected Ar count rate is  $\sim 5\%$  varying from one spacecraft pointing to the next.

We define the “soft colour” as the ratio of the background subtracted and deadtime corrected count rate in band 2 to that in band 1; the “hard colour” is the ratio of band 4 to band 3. This choice of colours gave the most separated normal and flaring branches in the colour-colour diagram.

There are systematic uncertainties in determining the colours. Uncertainties in determining the background result in changes of  $<0.14\%$  in the soft colour and  $<4.7\%$  in the hard colour. The colours as measured for the Crab are lower using the thin windowed detectors than using the thick

windowed ones (Kuulkers *et al.* 1994, Kuulkers 1995). On 20 Aug (day 232) 1985, just a few days before the Aug 1985 observations, detector 3 of array half 1 failed (Haberl 1992). This was a thin windowed detector and so there is a marked increase in measured soft colour after the failure. The increase was 2.5% for the Crab and  $\sim 1.5\%$  for GX 5-1. There are also changes of about 1% in both the soft and hard colours due to small changes in relative detector gains.

### 2.1: Determining the Z-track position: $S_Z$ .

The tight correlation of all source properties with position along the Z-track, and so by inference with  $M$ , suggests that it is reasonable to measure all observables as a function of Z-track position. This was first done using a “rank number” by Hasinger *et al.* (1990). Separate observations were ranked according to position. Because the HB/NB (hard) and the NB/FB (soft) vertices marked state changes these were assigned special rank numbers. The measurement of Z-track position was refined by Hertz *et al.* (1992) who fitted a tilted paraboloid and measured the Z-track position as an arc away from the NB/FB vertex. Here, we extend the measurement of position along the Z to arbitrarily shaped tracks. We develop an automatic and reliable method to separate data on closely spaced branches. We introduce a normalization which makes it easier to compare the Z tracks of different sources.

The position within the Z of each point in the colour-colour diagram was parametrized by drawing a smooth curve through the colour-colour points, and projecting the points onto this curve. The smooth curve was defined by choosing, by hand, normal points in the CD. These normal points were ranked. Two cubic spline fits were then made, one for each colour, between rank and colour. The two resulting splines form a numerical representation of the Z track in the colour-colour plane.

For each colour-colour point,  $P$ , an initial position on the Z track was defined as the point,  $Q$ , on the track closest to  $P$ . The arc length along the Z track between  $Q$  and the normal/flaring branch vertex was calculated. The NB/FB vertex was chosen as a reference point because it is the most clearly defined: it is the point on the Z track with the lowest soft and hard colours. The arc length between  $Q$  and the NB/FB vertex depends upon the scale of the CD, which in turn depends upon the choice of energy bands. The parameter  $S_Z$  was defined as the arc length along the Z normalized such that the HB/NB vertex corresponds to  $S_Z=1$  and the NB/FB vertex to  $S_Z=2$ . Our definition of  $S_Z$  is similar to that of “rank number” of Hasinger *et al.* (1990) in that the values 1 and 2 are assigned to the vertices, and to that of “ $s_z$ ” of Hertz *et al.* (1992) in that we use arc length along the Z track to determine position. Following Hertz *et al.* (1992) we call the distance between  $P$  and  $Q$ , normalized in the same fashion as  $S_Z$ ,  $D_Z$ . So, the above procedure basically transforms the two colour coordinates (soft and hard colour) into the two coordinates  $S_Z$  (distance along the Z track) and  $D_Z$  (distance perpendicular to the Z track).

When comparing Z-track positions from different detector and different sources there are unavoidable dependencies upon the choice of energy bands used, the detector response and the source’s energy spectrum. With our normalization these dependencies are much reduced; the major factor remaining is the relative ranges of the colours. In our case the ranges are nearly equal.

In determining  $S_Z$  there is a complication. As can be seen from Fig. 1, the normal and flaring branches are relatively close together. The statistical uncertainties are sufficient that some colour-colour points which belong on one branch, are actually closer to the other branch. At the 196-sec integration time that we used in Fig. 1 such wayward  $S_Z$  measurements are rare and therefore easily identified. However,  $S_Z$  shows changes on time scales less than few hundred seconds which are smeared with 196-sec integrations. In an attempt to follow these faster changes in  $S_Z$ , we also used shorter (16 and 32sec) integration times. Then, due to the larger statistical errors, the procedure outlined above created two sets of  $S_Z$  values, the majority corresponding to the branch on which Sco X-1 actually was, and the other set incorrectly attributed to the adjacent branch. Because of the rough symmetry about the vertex, the two sets of  $S_Z$  values approximately mirrored each other about the line  $S_Z=2$  when plotted against time. We tested several automatic methods to identify the wrongly assigned points and move them back to the correct branch.

We first tried to identify wayward  $S_Z$  values by finding values that were more than a set number of standard deviations from the mean of their time-wise neighbours. The local standard deviation

and mean of  $S_z$  were calculated from the nearest 3–5 neighbours on each side of the value being tested. Using this method, it was possible to distinguish isolated wayward points, but the method totally failed when there were 3 or 4 wayward points close together in time. We then experimented with a method where each 16 or 32-sec  $S_z$  value was compared with a linear interpolation between the 196-sec values. This method was more effective as it was very good at identifying mis-assigned points, but it often smoothed out short ( $\sim 600$  sec) but real changes in position on the Z track. The method we finally settled upon, used the *mode* of groups of usually 12 consecutive 16 or 32-sec  $S_z$  values to determine the long-term trend. Each  $S_z$  value that was more than  $3\sigma$  from the long-term trend was identified as wayward. The standard deviation  $\sigma$  was determined from the scatter of all 16 or 32 sec points around the long term trend.

For each colour-colour point, P, there are up to three possible positions upon the Z track, corresponding to three local minima in the distance between the point and the track. As described previously, initially the  $S_z$  value corresponding to Q, the closest position on the Z track (corresponding to the global minimum) was used. If a point was identified as wayward, then of the three possible  $S_z$  values the one closest to the long term trend was selected to replace the initial value. This checking and replacing procedure could be done recursively. Generally only one iteration was necessary.

The scaling of the  $S_z$  values was provided by measuring the arc length between the HB/NB and the NB/FB vertices. The position of the NB/FB vertex could be accurately pin-pointed because it corresponds (by definition) to a minimum in both colours and because of the local symmetry of the Z-track about the vertex. The position of the HB/NB vertex ( $S_z = 1$  in Fig. 1) is harder to determine than that of the NB/FB vertex because it is more rounded. The process used to find the initial, uncorrected  $S_z$  values led to clustering of points on the convex side of the vertex, near the inflection point of the smooth curve. This is a geometric effect that, incidentally, is markedly reduced by the procedure used to reassign wayward  $S_z$  values. This clustering was used as a further measure of the NB/FB vertex position and was used to define the exact arc length of the HB/NB vertex. Its position is in the region expected from the changes in the power spectra.

## 2.2: Power Spectra.

All (primarily Xe) data with 31.25 ms or better time resolution were divided into segments of 16 or 32 sec in length with no data windowing applied. Power spectra, normalized as per Leahy *et al.* (1983) were calculated from these data segments using the FFT algorithm. These segments had 4096, 2048 or 1024 data points depending on time resolution. These were combined into dynamical power spectra binned in frequency to a resolution of about 0.25 Hz. The evolution of the QPO could be followed in these dynamical power spectra.

The power spectra were averaged over hand-picked contiguous sections of the data where both count rate and  $S_z$  were constant to within 10%. Sometimes, when the count rate was changing too rapidly for this, the data were split into sections that reflected the nature of the variation. For example, in a flare, one or more sections covered the rise, one covered the peak, and one or more covered the decline. The aim of splitting up the data in this fashion was to increase sensitivity to any count rate or  $S_z$  dependent changes in the QPO.

When QPO were present in the dynamical power spectrum, the average power spectra were fitted over the 2–40 Hz range with a Lorentzian representing the QPO peak plus a constant level representing the white noise (“Poisson noise”) and any other broad-band components in that frequency range. The power spectra of data sections near (in time or count rate) those with obvious QPO were examined for possible QPO peaks. Any suspected QPO peak was fitted. However, the resulting fit was rejected if the QPO peak(s) was not significant.

We then performed a second power spectral analysis, aimed primarily at measuring the non-QPO power spectral components. In order to make it possible to measure the VLFN component, we used 128-sec long data segments in this analysis. No data windowing was applied. The original full time resolutions were used so that the extent of the HFN could be ascertained as well as possible. From the fits to the average power spectra of the 16 or 32-sec data segments, the  $S_z$  range where QPO were evident was already clear. The power spectra calculated from 128-

sec segments from outside this range, so without QPO, and which had similar  $S_z$  values, were averaged. In averaging, each power spectrum was given a weight proportional to how much it overlapped, in time, with the chosen range in  $S_z$ . These averaged power spectra were fitted with a model consisting of a VLFN (power law:  $\nu^{-\alpha_{VLFN}}$ ) and an HFN (exponentially cut-off power law:  $\nu^{-\alpha_{HFN}} e^{-\nu/\nu_{cutHFN}}$ ) component. When a fit's reduced  $\chi^2$  value was high and the residuals indicated a further component, a fit function containing an extra LFN (cut-off power law) and/or Lorentzian component was fitted. The white noise level in all these fits was fixed at the level predicted by the theoretical deadtime effect on the Poisson noise (see Sect. 2.3).

In those 128-sec intervals where QPO were evident, we performed fits with a full VLFN+ HFN+ QPO model. We found that selecting data by  $S_z$  was not sensitive enough to freeze changes in QPO frequency near the vertex or along the FB. Using the fits to the power spectra of the 16 or 32-sec data segments as a guide, power spectra from the 128-sec segments where the QPO frequency was the same to within 1 Hz were selected and then averaged. No LFN or extra QPO component were warranted.

In all these fits, the functions describing QPO and broad band noise components were normalized by their total power as measured over a wide frequency range (see van der Klis 1995a for the specific formulae). The advantage of this approach is that the integral power is directly fitted to the power spectra and its error follows directly from a scan in  $\chi^2$  space.

### 2.3: Deadtime Effects.

The four-band (I7) data and the high time resolution (T3 and T5) data are affected by different deadtime processes. In both cases 0.5% of the incident counts are lost due to the electronic chain coincidence logic deadtime. Beyond this, the HTR count rates suffer from only the constant detector deadtime of  $5.5 \mu\text{sec}$  (Andrews and Stella 1985, but see below). This sort of deadtime process results in a correlation between successive time bins which results in a rise in predicted Poisson noise power toward the Nyquist frequency. In spite of the high count rates in some of our observations, this frequency dependence of the Poisson noise power spectrum was found to be always completely negligible. The frequency averaged Poisson noise was calculated using formula (3.9) of van der Klis (1989) for each individual power spectrum. When power spectra were averaged the expected Poisson levels were also averaged with the same weighting.

The accuracy of the estimated Poisson level is limited by the accuracy to which the ME detector deadtime is known. Using data from a wide variety of X-ray sources Berger & van der Klis (1994) found that for T3 and T5 data, the high frequency ( $\geq 256 \text{ Hz}$ ) noise level at a given count rate could be best fit with a deadtime of  $10.6 \pm 0.3 \mu\text{sec}$  rather than  $5.5 \mu\text{sec}$ . This means that the strength of the HFN is underestimated in our analysis by 0.3–0.4% (rms). Observations of Cyg X-3 (Berger & van der Klis 1994) and a comparison between the HFN strengths as measured with EXOSAT and Ginga for various Z sources (Prins & van der Klis 1997, Berger & van der Klis 1998) further suggest that there is extra noise in the EXOSAT ME observations at a level of  $\sim 3.3\%$  (rms) with a cut-off frequency near 100 Hz. If this noise is an instrumental effect of the EXOSAT ME and if it is the same for the Ar and Xe detectors, then the rms amplitudes of the HFN reported below are overestimated by about 0.5% (rms). Note that the two effects approximately cancel in our case. The effect of these instrumental details on other power spectral components than the HFN is negligible.

In the case of the HER data modes (which include HER7, the source of the I7 data) the basic deadtime process is one in which not more than one photon can be detected in each  $1/4096$  sec long time-sample. Andrews and Stella (1985) derived an accurate, within  $\leq 0.1\%$ , expression (their equation 2) for the count rate correction factor, which we used to correct the count rates in each channel before calculating the colours. In the cases where we used I7 data for calculating power spectra, we applied the empirical deadtime corrections determined by Kuulkers *et al.* (1994, 1997) to estimate the Poisson level.

All quoted QPO amplitudes have been corrected for differential deadtime effects (Lewin, van Paradijs & van der Klis; 1988) and for the effects of time binning (van der Klis 1989). Differential deadtime occurs when the deadtime depends upon count rate and so the deadtime is larger in the

peaks than in the valleys of a signal. Hence, the count rate is suppressed by a larger factor in the peaks. The end result is the rms amplitude goes down. The rms amplitudes of the other power spectral components have also been corrected for differential deadtime effects but not for the loss of sensitivity due to time binning. In the only case where the binning effect is not negligible (the HFN), the loss of sensitivity near the Nyquist frequency is partially compensated by an unknown amount of power aliased from beyond the Nyquist frequency.

### 3: Results

#### 3.1: Overall Behaviour.

The colour-colour diagram of Fig. 1 is made up from the five EXOSAT observations performed in 1985–86 where Ar four-channel I7 data were available. The diagram shows a single Z pattern with data from 1985 and 1986 overlapping on the lower NB. These observations were made under nearly identical conditions (e.g. collimator response) and so the primary uncertainties in the position of the Z-track from one observation to the next are due to changes in the background and detector gain changes. Background uncertainties could result in a 1% change in the soft colour and a 10% change in the hard colour. Using the Crab as a calibrator the gain changes in Array Half 1 (the only half used) during 1985 were about 1% in both the colours. These uncertainties should be compared with the shifts seen for Cyg X-2;  $\sim 3\%$  in soft colour and  $\sim 8\%$  in hard colour Hasinger (1987b), Kuulkers *et al.* (1996) and for GX 5-1; 11% in soft colour and  $\sim 7\%$  in hard colour Kuulkers *et al.* (1994).

Observations made in 1984 show a Z track that is slightly shifted in both colours and with a subtly different shape (see Fig. 2). The about 5% drop in hard colour of the NB/FB vertex visible in Fig. 2 with respect to Fig 1 is within the systematic uncertainty. The 1984 observations were made under significantly different conditions from the latter I7 (1985/86) observation. Between the two sets of observations detector 3 of array half 1 failed. Using the Crab as a calibration source and cross checking with GX 5-1 (Kuulkers *et al.* 1994, Kuulkers 1995) we found that the loss of detector 3 and small gain changes between 1984 and 1985 are expected to result in a 2–3% increase in the measured soft colour. This is contrary to the measured  $\sim 1.5\%$  decrease in soft colour between the 1984 and 1985/86 observations. However there are several other effects that will influence the soft colour, which can not be adequately calibrated using the Crab. These effects include the different energy boundaries used for the Sco X-1 observations, the different energy spectrum of Sco X-1 as compared to the Crab and GX 5-1 and the low collimator responses of the all Sco X-1 observations. Also the collimator responses are larger for 1984 (12%–23%) than for 1985/86 (8%–12%). These other effects could explain the differences between the 1984 and the 1985/86 observations and so there is no evidence for from these data for secular changes in the Z-track of Sco X-1 between 1984 and 1985/86. In the period 1985/86 we can only exclude only the largest secular changes seen in GX 5-1 (Kuulkers *et al.* 1996).

Because of the differences in their Z tracks, the 1984 and the 1985–86 data were treated separately. The  $S_Z$  values were calculated as described in Sect. 2.1 independently for the two data sets. The  $S_Z$  scaling of the 1985–86 data, where both the HB/NB and NB/FB vertices are seen, was also applied to the 1984 data, where only the NB/FB vertex is present.

On all hardness-intensity diagrams produced from the 1985–86 (HER7) and 1984 (HER5) data, the minimum hardness (colour) was found to correspond to minimum brightness. So, the point  $S_Z=2$ , which was set at the minimum in both the soft and hard colours on the CD should also correspond to minimum brightness. Fig. 3 shows this is the case for the 1985–86 data. A similar variation in count rate with  $S_Z$  is found for the 1984 data. Fig. 3 clearly shows that the count rate is not a good indicator of  $S_Z$ , and by inference the mass accretion rate.

The count rate versus  $S_Z$  plots provide a check on the accuracy with which we can fix the position of the NB/FB vertex upon the CD. We fitted count-rate/ $S_Z$  data in the region near the vertex with two intersecting straight lines. For the 1985–86 data there was no measurable difference between the position of minimum count rate and the  $S_Z=2$  position. However, for the 1984 data the count rate reaches its minimum slightly NB-ward of the NB/FB vertex, at  $S_Z=1.978$ . We have shifted the  $S_Z$  values of the 1984 data by  $\Delta S_Z = 0.022$  to match them with the 1985–86 data.



This small discrepancy gives an indication of how well the position of the NB/FB vertex can be placed. Most of this difference can be accounted for by the uncertainty in determining the placement of the NB/FB vertex rather than from effects arising from having slightly different energy bands and different detector responses between the two data sets. Because the HB/NB vertex is more rounded the uncertainties in its placement are larger. We estimate that the uncertainties in placing the NB/FB and HB/NB vertices are  $\pm 0.013$  and  $\pm 0.05$   $S_Z$  units respectively. This leads to a uncertainty of  $\sim 5\%$  in the scaling of the Z-track, The errors on individual  $S_Z$  values are much larger being the projection of the statistical errors of the individual colour measurements (See Fig 1).

Fig. 4 shows various representative power spectra in the Xe (*filled circles*) and Ar (*open squares*) energy ranges; the drawn lines are model fits. The spectra are all plotted to the same scale and normalized such that the power density is in units of  $(\text{rms}/\text{mean})^2/\text{Hz}$  (see van der Klis 1995a for the formulae). The estimated Poisson level has been subtracted, and the spectra have been corrected for differential deadtime effects (van der Klis 1989b), but not for time binning and aliasing. The segment of the Z track corresponding to each power spectrum has been indicated in Fig. 1.

In broad terms, the features of these power spectra are similar to those noted by HPM89 and Hertz *et al.* (1992). The rms amplitude of the VLFN increases along the Z track (Fig. 4A to F; note the layout of Fig. 4; it reflects the shape of the NB-FB part of the Z track), while that of the HFN decreases. No QPO are observed in the HB (the 90% confidence level upper limit in the Xe band is 3% rms), but the peaked LFN is obvious (Fig. 4A). Detailed analysis shows that the LFN persists into the upper NB. The LFN is just visible in Fig. 4B. At positions just before the QPO appear ( $S_Z = 1.5$ ; not shown as a separate plot in Fig. 2) only VLFN and HFN are detected. The high time resolution and high count rate of the data make it possible to trace the HFN out to high frequencies. In the lower NB (Fig. 4C) the well known 6 Hz QPO (the NBO) is evident. Upon entering the FB (Fig. 4D) the QPO frequency increases. The highest FBO frequency measured is 21 Hz. Further along the FB (Fig. 4E) there is some evidence for an additional peaked component near 5.5 Hz. Higher still on the FB (Fig. 4F) there is only strong, steep, VLFN and relatively weak HFN.

A comparison between the Ar and Xe power spectra clearly shows the strong energy dependence of the various components. The fractional rms amplitudes of all components are larger, by up to a factor of 3 (9 in power), in the higher Xe energy band. The strong energy dependence of the FBO strength we report here is a new result. In Fig. 4D there is only a slight indication of any FBO (15 Hz) in the Ar data, while they are easily visible in the Xe data; the difference in fractional rms amplitude is a factor of 2.5. Table 2 gives the fractional rms amplitudes of the various components for both the Ar and Xe power spectra of Fig. 4.

### 3.2: The broad band noise components: VLFN, LFN and HFN.

In Fig. 5, we present the best fit parameters of the VLFN, LFN and HFN obtained from the 128-sec Xe power spectra selected as described in Sect. 2.2. Two sets of fits were performed; one with the HFN slope ( $\alpha_{\text{HFN}}$ ) fixed at zero, the other with this parameter free. In most fits where  $\alpha_{\text{HFN}}$  was a free parameter, it is slightly positive, but consistent with being zero at the  $2\sigma$  level. When  $\alpha_{\text{HFN}}$  was fixed to zero the  $\chi^2$  value increased, but usually not significantly, nor did the other fit parameter values change significantly. For ease of comparison with other studies, the values reported in Fig. 5, except those of  $\alpha_{\text{HFN}}$ , are those obtained from the fits with  $\alpha_{\text{HFN}} \equiv 0$ .

The VLFN rms amplitude integrated over 0.001–1 Hz increases monotonically from 1.0% in the HB to 25% in the upper FB (the  $2\sigma$  lower limit there is 18%). The VLFN is stronger in the Xe band than in the Ar band on the NB and FB, but on the HB the difference is small (see Table 2 and Fig. 4). However, as the VLFN is very weak on the HB and only evident in the one or two lowest frequency points, the determination of the VLFN parameters there is uncertain. The VLFN power law index ( $\alpha_{\text{VLFN}}$ ) is lowest on the HB, increases from 1.2 to 1.7 along the NB, and is constant on the FB. The mean FB value is  $1.76 \pm 0.04$ , practically the same as that measured by Hertz *et al.* (1992),  $1.72 \pm 0.01$ . Several of the individual power law index measures, especially along the FB, are close to 2. There may be some low frequency leakage (Deeter 1984) from the 5–35 min duration,

10-200% flares on the FB.

The LFN appears as “peaked noise” in the HB. The amplitude in Xe is highest (3.3% rms) at the lowest observed  $S_Z$ , drops when Sco X-1 enters the upper NB, and further along the Z track ( $S_Z \geq 1.5$ ) it is undetectable with a 97.5% confidence upper limit of 2% rms. Both the LFN slope and cut-off frequency change rapidly near the HB-NB vertex. The slope,  $\alpha_{LFN}$ , changes from  $-1.5$  to about  $0.0$  there, while  $\nu_{cut}$  increases from about  $1.4$  to  $>7$  Hz. These steep dependencies on  $S_Z$  reflect a broadening of the LFN shape.

The HFN amplitude (integrated over 1–500 Hz) gradually decreases from the HB (8.4%) to the FB (5.5% rms). The weighted average of all measurements of the power law slope of the HFN is  $0.066 \pm 0.001$ , indicating an on average slightly “red” noise shape for this component. The apparent dip in  $\alpha_{HFN}$  near the NB/FB vertex is not very significant: the average  $\alpha_{HFN}$  in the range  $1.8 < S_Z < 2.2$  is only  $2\sigma$  less than the overall average. We do find two significant features in the variation of the HFN cut-off frequency with  $S_Z$ . The cut-off frequency drops from  $\sim 70$  on the HB to  $\sim 35$  Hz ( $4.4\sigma$  difference) on the NB, and then increases along the FB to about 100 Hz (95% confidence). This last trend seems to be at odds with the results of Hertz *et al.* (1992), who found that the width of the half Gaussian they used to fit the HFN decreased as Sco X-1 moved up the FB.

The amplitude of the HFN is, at similar positions on the Z track, consistently  $\sim 4\%$  rms higher than that measured by Hertz *et al.* (1992) using Ginga. This difference can be explained by the difference in energy response of the two detectors. The EXOSAT Xe detectors are more sensitive to higher energies, where the HFN is stronger, than the Ginga LAC. A similar difference in amplitude is found for the VLFN component.

The HFN is detectable above the noise out to about 300 Hz in the upper NB and to at least 100 Hz in the FB (Figs. 4A, B and E). In these regions the source count rate is highest, making the HFN more readily detectable against the Poisson noise level. As discussed in Sect. 2.3, uncertainties in the instrumental effects on the power spectrum make these estimates uncertain.

### 3.3: The NB-FB QPO.

The results of the QPO fits to power spectra of the 16 and 32-sec data segments averaged together over intervals of constant count rate or  $S_Z$  as described in Sect. 2.2 are displayed in Figs. 6 & 7.

QPO are detected ( $\geq 2.0\%$  rms) over only a small part of the Z track ( $S_Z = 1.5\text{--}2.2$ ), or only  $\sim 17\%$  of the total  $S_Z$  range. NBO occur on only the lowest one third of the NB while FBO occupy only the lowest 10% of the FB. The QPO are weaker in Ar than in Xe on both the normal and flaring branches.

Previous studies have shown that as the QPO frequency increases the width increases in step keeping the relative width roughly constant. The relative width varies is the inverse of the QPO coherence. By binning in  $S_Z$  (Fig. 6) we reveal that there are systematic changes in the relative width ( $\Delta\nu/\nu$ ) along the Z-track. It is lowest ( $\sim 0.27$ ; highest QPO coherence) in the lower NB ( $S_Z=1.75$ ), and increases on the FB (to  $\sim 0.41$  at  $S_Z=2.05$ ) and possibly in the upper NB. The coherence time-scale ( $\tau_{coh} \equiv 1/\pi\Delta\nu$ ) ranges from  $\sim 0.18$  sec (1 QPO cycle at 6 Hz) in the NB to  $\sim 0.05$  sec (0.75 QPO cycles at 15 Hz) in the FB.

In Fig. 7, showing the results of individual fits to each data section with QPO, the symbols refer to same observations as those in Fig. 1. Figs. 7a and 7b show the dependence of NBO/FBO fractional rms amplitude on  $S_Z$  using the combined Ar+Xe (1984) and Xe only (1985–86) data. The QPO are weaker in the lower energy Ar band than in the Xe band on both the normal and flaring branches. In both energy bands the QPO amplitude increases with  $S_Z$ . In the Xe only data, which spans a greater range of  $S_Z$ , a clear increase in fractional rms amplitude is seen along the NB, from  $\sim 3\%$  at  $S_Z=1.55$ , to  $\sim 5\%$  at  $S_Z=1.95$ , and up to 8% in the FB. In the lower energy Ar+Xe data, the QPO fractional rms is about 2.5% in the lower NB and between 2 and 4%, but usually  $>3\%$  in the FB. In the higher count rate Ar+Xe data there is a steep increase in QPO rms amplitude (1% rms within 0.05  $S_Z$  units) at the NB/FB vertex. There is possibly a similar steep increase (2% rms

within 0.05  $S_Z$ -units) of the QPO amplitude in the Xe band data. But in view of the large scatter in measured rms amplitudes on the FB, the identification of steep changes in rms amplitude at the NB/FB vertex is only tentative.

Clearly there is a dramatic jump in the QPO frequency at the transition from the NB to the FB (Fig. 7c). The actual transition is not resolved. It occurs within a span of  $\leq 1.5\%$  of the Z track, or  $\leq 8\%$  of the span over which QPO are detected. The QPO frequency is between 5.5 and 7 Hz all the way along the NB from  $S_Z=1.5$  to  $S_Z=1.9$ . At  $S_Z=1.95$  the QPO frequencies are between 6.4 and 8.5 Hz, and at  $S_Z=1.98$  between 6.5 and 12 Hz. The average frequency is  $\sim 8$  Hz here. Upon entering the FB ( $S_Z \geq 2$ ) the average QPO frequency jumps from  $\sim 8$  Hz to  $\sim 12$  Hz, and then increases more gradually with  $S_Z$  and brightness. The highest frequency measured ( $\sim 21$  Hz) was during a flare in the Feb 1985 data.

A frequency-intensity diagram of the 1985-86 Xe, data sets is shown in Fig. 7d. For the Xe+Ar data this diagram looks qualitatively the same but at higher count rates. The same features as in the frequency versus  $S_Z$  diagram are visible. By also using high time resolution count rate data for which there are no simultaneous energy resolved data, (included in Fig 7d but not Fig 7c) we find that the average frequency increases slightly but significantly along the upper NB as Sco X-1 approaches the NB/FB vertex. As the count rate changes from 3000 to 2450 cts/sec/8 detectors, corresponding (using the count rate vs  $S_Z$  relation) to  $S_Z=1.57$  and 1.87, respectively, the average QPO frequency increases from  $5.96 \pm 0.04$  Hz to  $6.30 \pm 0.03$  Hz.

On both the frequency- $S_Z$  and frequency-intensity diagrams there is more scatter on the lower NB near the transition and on the FB than on the upper NB. This is evident in the dynamical power spectra (16 or 32 sec time resolution), which show the band of NBO powers becoming broader and more diffuse near the NB/FB transition. Near the NB/FB vertex the QPO frequency is more sensitive to  $S_Z$  than in other places on the NB, while on the FB the QPO frequency is changing on the same time-scale as the flares, i.e., minutes to hour(s). In both cases the time-scale of the changes in QPO frequency becomes comparable or shorter than the typical integration times ( $\geq 200$  sec) used to fit the QPO and measure the position on the Z track. The  $S_Z$  values become difficult to measure on time scales  $< 200$  sec. Some of the scatter on the frequency- $S_Z$  diagram can therefore be explained by the increased difficulty in measuring  $S_Z$ , but this does not hold for the scatter in the frequency-intensity diagram. Here the extra scatter could be intrinsic to Sco X-1, indicating either the presence of hysteresis or the influence of a another variable besides  $\dot{M}$  on QPO frequency and/or brightness. Direct tests for hysteresis are made in Sect. 3.6 and a careful examination of the QPO behaviour during normal/flaring branch transitions (Sects. 3.4 and 3.5) finds evidence for the effects of an additional variable.

### 3.4: Normal/Flaring Branch Transitions.

Upon examination of Fig. 7 and the dynamical power spectra we found that there are three QPO frequencies that are important in the description of the different modes of behaviour of Sco X-1. At frequencies  $< 7$  Hz Sco X-1 is on the NB and there are only weak correlations between  $S_Z$ , QPO frequency and count rate. Overall as  $S_Z$  increases the QPO frequency increases and the count rate decreases. Between 7 and 8 Hz Sco X-1 is on the lowest part of the NB ( $S_Z > 1.9$ ) and there is a positive correlation of frequency with  $S_Z$ , but an inverse correlation with count rate. As Sco X-1 makes the transition between the NB and FB the QPO frequency changes from 8 to 12 Hz. Here the relation between frequency and position cannot be exactly determined with the current data. Above  $\sim 12$  Hz Sco X-1 is on the FB, where there is a strong positive correlation between QPO properties,  $S_Z$  and brightness. We use these three QPO frequencies (7, 8, 12 Hz) to discuss the different time scales on which the QPO frequency changes near the NB/FB vertex.

In the following discussion of the QPO behaviour keep in mind that we could not reliably measure the QPO frequency on time scales less than  $\sim 200$  sec. By also considering the count rate behaviour we can sometimes deduce that the QPO frequency must have changed rapidly between two adjacent sections of data. The shortest time-scale measured in this way for a significant change in QPO frequency is 90 sec. We cannot make any general statements on frequency variations faster than this. In most cases we found that the changes in QPO frequency took the same time no matter in which direction Sco X-1 was traveling on the Z track.

Based upon a careful examination of the dynamic power spectra, intensities and colours we find that one can distinguish four patterns of behaviour near the NB/FB vertex.

- I *Grand Transitions*. These are very obvious steady transitions between the NB and the FB or vice-versa. This is the sort of transitions described by Priedhorsky *et al.* (1986). These transitions separate the historical active and quiescent states which correspond to the FB and NB respectively. On the FB side of a *grand transition* Sco X-1 shows classic flaring behaviour. During flares, count rate changes of up to a factor of two occur on time scales of minutes to tens of minutes. Each flare represents a movement up and down the FB with associated changes in brightness, colour(s), QPO frequency and other power spectral parameters. On the NB side there are no flares, but slower, tens of minute to hours time-scale changes in  $S_z$ . Here the brightness changes are less than a factor of 2 and the QPO frequency varies between 5.5 and 8 Hz. Within the EXOSAT data set we have found 5 *grand transitions* which are indicated in the “Branch” column of Table 1. During these transitions Sco X-1 moves continuously and smoothly (i.e., with no reversals in the direction) in the CD, HID and frequency-intensity diagram. The change in QPO frequency involved in a *grand transition*, i.e., from  $\sim 7$  Hz to  $>12$  Hz or vice-versa, takes  $\sim 600$ – $1000$  sec. The speed with which the frequency changes is different over different frequency intervals. The change from 8 Hz to  $>12$  Hz or vice-versa is most rapid, taking between  $<120$  sec and 300 sec, while the frequency change between 7 and 8 Hz usually takes  $\sim 300$  to  $\sim 700$  sec. On either side of the transition the frequency changes are more gradual. On the NB frequency changes in the range 5.5 to 7 Hz take typically many hundreds of seconds while on the FB the time-scale of the frequency changes is the same as that of the flares.
- II *FB dips*. On the FB, during relatively brief ( $<200$ – $600$  sec) periods of lower count rates, FB QPO appear. This is the sort of behaviour that was noted by van der Klis *et al.* (1987). We have found tens of these dips in several observations. In all cases the frequency never dropped below about 10 Hz, so there are no switches to NBO. The change in frequency between 15 and 10 Hz can take less than 120 sec.
- III *NB dips*. On the NB, there are also relatively brief ( $\sim 600$  sec) dips in count rate as the QPO frequency increases to 8–9 Hz before returning to the norm of 5.5–6.5 Hz. Sco X-1 does not enter the FB proper during these episodes. The *NB dips* can be thought of a sub-group of the *rapid excursions*.
- IV *Rapid Excursions*. These are rapid changes in frequency from  $\sim 7$  Hz to  $>12$  Hz, i.e. well into the FB, and back. We found 8 rapid excursions in the entire high time resolution data set, i.e., 3 Aug 1984 (2), 25 Feb 1985 (2), 25 Aug 1985 (1), 27 Aug 1985 (3). They all started and ended in the NB. Usually the change from 7 to  $>12$  Hz took  $\sim 120$  sec, but in one case it took less than 90 sec. The return to the NB (from 8 to  $\sim 6.5$  Hz) is generally slower; 300–600 sec. This sort of behaviour has not been previously described.

When Sco X-1 moves through the NB/FB vertex, the count rates and colours reach a minimum when the QPO frequency is near 8 Hz. These conditions define the NB/FB vertex. Thus, in an excursion from NB to FB and back the count rates and colours should pass through two equal depth minima, each time as the frequency passes 8 Hz. In between these two minima, the count rates and colours reach a maximum as the frequency reaches its peak value. Just before making a transition, i.e., when the QPO frequency is near 7.5 Hz the Xe count rate, soft and hard colours are 2220–2360 counts/second/8 detectors,  $0.903 \pm 0.007$  and  $0.661 \pm 0.009$  respectively (all uncertainties in this paragraph correspond to the observed total scatter). During the transition, the hard colour is more sensitively dependent on  $S_z$  on the NB side of the vertex, while the soft colour is more sensitive on the FB side of the vertex. At the vertex the minima are located in Ar count rate at  $4108 \pm 112$  counts/second/8 detectors (at 10% response; 1986 observations; see Sect. 2 for the issues to do with the Ar collimator response), in Xe count rate at  $2247 \pm 82$  counts/second/8 detectors, in soft colour at  $0.907 \pm 0.015$ , and in hard colour at  $0.650 \pm 0.015$ . On the FB side the count rate, soft and hard colours increase to 2230–2660 counts/second/8 detectors,  $0.91 \pm 0.01$  and  $0.663 \pm 0.005$ , respectively, when the QPO frequency reaches 15.5 Hz.

Examining the best-covered transitions on timescales ranging from 2–32 sec we find, using a  $\chi^2$  test for constancy, that even within individual observations there are variations in the depth of the count rate minima during NB/FB transitions beyond those expected from counting statistics (95% confidence). The full range in the depth variation is  $\sim 1\%$  of the count rate at the NB/FB vertex. By inference the colours at the NB/FB may also vary. Thus the vertex covers a range in brightness and possibly colours, with Sco X-1 traversing slightly different paths in the CD or HID as it moves between branches. In other words; the one-to-one correspondence between Z track position, measured by  $S_Z$  and other variables breaks down near the NB/FB vertex, suggesting that there is another parameter, in addition to  $\dot{M}$ , governing the behaviour of Sco X-1.

We found that in two of the *rapid excursions* Sco X-1 did *not* follow the standard behaviour when the QPO frequency went through an excursion from levels appropriate to the NB to higher values. These *anomalous frequency excursions* are discussed next.

### 3.5: Anomalous Frequency Excursions.

Two cases of anomalous frequency excursions were found during a careful examination of the entire high time resolution EXOSAT data set. The first example discovered, occurred on 13 Mar (day 72) 1986, is apparent in Fig. 7b,c,d, where two points (*circled*) on the NB in the CD and HID have higher frequencies ( $8.1 \pm 0.3$  Hz and  $11.1 \pm 0.5$  Hz.) and amplitudes (Xe band) higher than is usual for the NB. These frequencies and amplitudes are more appropriate to the FB, but the corresponding values of  $S_Z$ , near 1.9, place these points squarely on the NB. The dynamical power spectrum shows a fast increase and decrease in frequency with a total duration of  $\sim 5$  min. This sort of frequency behaviour is very similar to that of *rapid excursions*, but there is no change in the colours and consequently the derived  $S_Z$  values. The other instance of an anomalous frequency excursion is the looping behaviour first noted by van der Klis *et al.* (1987) on 30 Aug (day 242) 1983. Here, Sco X-1 executed a loop upon the frequency-intensity diagram, initially passing from the NB to FB through the NB/FB vertex but then returning **directly** to the NB, by-passing the vertex. Once again the dynamical power spectrum is very similar to that of a *rapid excursion* but the hardness and count rate do not show a peak, bracketed by two dips as the QPO passes through 8 Hz. The count rates, frequency, and colour behaviour during these two events was scrutinized in greater detail and compared to what is found during standard NB/FB transitions.

The time-wise behaviour of Sco X-1 during the March 1986 frequency excursion is summarized in Fig. 8. Before the start time of this figure Sco X-1 was in the mid-NB (i.e., with lower  $S_Z$  values, higher colours and intensities than shown) and generally moving down the NB. Just after  $1.5 \times 10^4$  sec we see that the QPO frequency reaches a maximum value of  $\sim 16$  Hz. This point is labeled “Peak” in Fig. 8. At the same time the count rates from the Ar and Xe detectors reach a maximum. At this point the QPO frequency and count rates are typical of the FB. About 270 sec before, and  $\sim 1200$  sec after the peak in count rate and QPO frequency there are two dips in the counting rate, at the same time as the QPO frequency passes through 8 Hz. Both dips are labeled as such in Fig. 8.

At the time of the count rate dips there are two marginal drops in the colours; see top two panels of Fig. 8. As discussed above, the changes in the colours are expected to be small, with the change from minimum to the values corresponding to 16 Hz QPO being  $0.03 \pm 0.025$  (full range) for the soft colour and  $0.013 \pm 0.02$  (full range) for the hard colour. Changes of this size might be present in Fig. 8. At the first dip the  $S_Z$  values increase reflecting the small decrease in both colors, but then, instead of rising to values  $>2$  as would be appropriate for a rapid change to the FB,  $S_Z$  drops again. At this time the colours do not vary in unison which explains the  $<2$  values for  $S_Z$ . The values of  $S_Z$  at this time, were not modified during the search and replace procedure used for wayward  $S_Z$  points (Sect. 2.1). To show the changes in colour more clearly we calculated a hardness ratio using the Ar and Xe band counting rates. The resulting hardness ratio (colour) is plotted in the middle of Fig. 8. There are clearly two dips in the hardness ratio flanking a general rise in hardness but the Ar/Xe colour does not track the count rates and QPO frequency closely as expected.

The observed pattern, a peak in count rate, QPO frequency and, marginally, colours bracketed by two dips associated with 8 Hz QPO, is just what is seen during *rapid excursions*. What is

not normal during this frequency excursion is the behaviour as the source moves to and from the peak in count rate and frequency as seen from the trajectories traversed on frequency-intensity, frequency colour(s) and colour-colour diagrams, which we discuss next.

The frequency-intensity diagram of Fig. 9 is similar to that of Fig. 7d but with higher time resolution during the frequency excursion, shows how the count rate varies before and after the peak QPO frequency. The 1986 frequency excursion is displayed as a dotted line, beginning at the point labeled ‘Start’, then moves via the ‘1st Dip’ to the ‘Peak’, then returning to near the NB/FB vertex at the ‘2nd Dip’ just before reaching the ‘End’ point, after which Sco X-1 remains on the NB. Clearly, in this diagram Sco X-1 does not follow the usual path between the normal and flaring branches. Both count rate dips are at comparable intensities to other observations when Sco X-1 was near the NB/FB vertex, but the subsequent movement to and from the peak in count rate and frequency seems to occur at an count rate that is  $\sim 200$  cts/sec/8 detectors higher than the standard path on a frequency-intensity diagram. This difference in count rate would correspond to an 8% difference in collimator response, or a 16 arcmin pointing offset between the 1986 and 1985 observation. We therefore checked if there was any motion in the pointing direction of EXOSAT during this observation or a difference in collimator response with respect to other observations. An examination of the house-keeping data showed stable pointing, and checking the original observational logs kept by ESA established that the Xe detectors were in all observations pointed directly at Sco X-1. Two hundred counts is far greater than the full range ( $\sim 26$  cts/sec/8 detectors) of the variations found in the background counting rates using observations spanning the years 1984–86. Examining the veto and guard count rates there is no indication of any change in the background at the time of the frequency excursion. The gain of the Xe detectors seems stable, since in all cases except the anomalous frequency excursions the Xe count rate at a particular  $S_z$  is reproducible over the lifetime of EXOSAT. We conclude that the different path taken in the frequency-intensity diagram during this excursion is intrinsic to Sco X-1.

This conclusion is supported by the frequency-colour diagrams. On both possible frequency-colour diagrams (Figs. 10a,b) the path of Sco X-1 is slightly shifted with respect to the other points in a similar way as on the frequency-intensity diagram. Such a shift cannot be caused by changes in the collimator response.

The motion on the colour-colour diagram of Sco X-1 during the frequency excursion is shown in Fig. 11. The position of the ‘1st Dip’ and ‘2nd Dip’ are marked by a filled circle and square respectively while the ‘Peak’ is marked with a filled triangle. The colour-colour points associated with the high QPO frequencies are surrounded on all sides and even coincide with points associated with 6 Hz QPO. At no time does Sco X-1 apparently enter the flaring branch. However, it should be noted that during the 1986 observations there were no standard transitions to the FB and so the FB data of Fig. 11 come from a year earlier. Therefore the frequency excursion could represent motion into a FB that is on top of the NB in the colour-colour diagram. We consider this possibility unlikely because the colour-colour diagrams appear stable from year to year. Observations well separated in time show that the positions of the NB and FB in the colour-colour diagram are reproducible, also the separation between the two branches shown in Fig. 1 using 1985–86 data is similar to that found in 1984 (see Fig. 2).

In summary, there are two possible ways to interpret what happened; Sco X-1 made a rapid excursion along a FB that is in an unusual place on the CD, or it remained on the NB while the QPO frequency changed briefly to values appropriate for the FB.

The second anomalous frequency excursion is seen as a loop on the frequency-intensity diagram (van der Klis *et al.* 1987) during the observations on 29/30 Aug (day 241/242) in 1983. The dynamic power spectrum is similar in appearance to a rapid frequency excursion. At the beginning of this observation the EXOSAT satellite pointing direction was moving. Although this movement apparently ended well before the unusual NB-FB-NB transition, the aspect information does not unequivocally show the pointing as being stable. So, it is possible (but in our experience unlikely) that the intensities are not entirely reliable. On this occasion the multi-channel data from the ME detector were affected by data overflows. Two-channel GSPC (Gas Scintillation Proportional Counter) data are available in the EXOSAT data base maintained at ESTEC and GSFC. The 5–8

and 8–15 keV light curves were extracted and a GSPC colour (hardness ratio) curve was calculated. The ME and GSPC data could be synchronized because the start times are recorded with better than 1 sec accuracy.

The time-wise behaviour during the loop is summarized in Fig. 12. Initial observations, ending 200 sec prior to the data of Fig. 12, show Sco X-1 on the FB. Sco X-1 was generally moving toward the NB/FB vertex. Judging by the colours and the QPO frequencies Sco X-1 was near the NB/FB vertex in the early part of the observation when the pointing was not stable. In fact Sco X-1 spends a long time (2000–3000 sec as opposed to the normal  $\sim 1000$  sec total duration for most transitions) near the vertex with a QPO frequency being between 8 and 12 Hz. As the frequency increases reaching a maximum of  $\sim 18$  Hz (labeled  $F_P$  in Fig. 12) there is an increase in the count rates (ME and GSPC) but no increase in colour, contrary to standard transition behaviour. This places Sco X-1 outside the FB on the frequency-colour diagram as delineated by the earlier measurements on the same day. As the QPO frequency decreases to near 16 Hz the count rates continue to increase to a maximum (labeled as  $I_P$ ). At this time the colours are increasing. Soon after the peak in count rate the frequency drops from 16 to 9 Hz (labeled Jump). During this abrupt drop in frequency there is no indication of a drop in either ME or GSPC count rates or colour as would be expected for a passage through the NB/FB vertex. Any such passage would have to be very rapid, say,  $< 30$  sec to go undetected in the light curves. The times most appropriate to be designated count rate dips are labeled A & B on either side of the frequency excursion. At A the colour is low but does not increase as the frequency becomes  $> 8$  Hz. At time B there is no indication of a change in colour. After the frequency jump, Sco X-1 moves toward the NB/FB vertex. At the very end of Fig. 12 there is a drop in colour and count rates which may indicate Sco X-1 approaching the NB/FB vertex. During the next ME observation, some 160 sec later (no GSPC data for 10660 sec) Sco X-1 is found in the NB with stable 6 Hz QPO.

Fig. 13 shows the colour-frequency diagram for Sco X-1 on 29/30 Aug 1983. Data from the three observation periods, separated by short (200 and 160 sec) intervals, are displayed with different symbols. In the first observation (*filled triangle*) Sco X-1 was on the FB. The third observation (*filled square*) finds Sco X-1 on the NB. During the middle observation (*filled circle*), covered in Fig. 12, Sco X-1 executes a large loop on the colour-frequency diagram. The positions of the maximum frequency ( $F_P$ ) and count rate ( $I_P$ ) as well as the positions of the count rate dips (A & B) are marked. Only point A is near the vertex. The jump between the FB and NB frequencies occurs within 120 sec with no indication of any drop in the colour or count rate that would indicate a passage through the NB/FB vertex.

We have checked the veto and guard rates and find no evidence for any change in the background at the time of the frequency excursion. Therefore we can conclude that Sco X-1 made either a very quick ( $< 30$  sec) transition from the mid-FB to the mid-NB, passing through the vertex too rapidly to be measured, or jumped directly between the flaring and normal branches.

The two anomalous frequency excursions presented in this section and the different brightness levels during NB/FB transitions discussed near the end of Sect. 3.4 represent the first evidence that a strict one-to-one relationship between spectral state and QPO behaviour does not hold on short (several 100 sec) time scales.

### 3.6: Movement along the Z track.

Using the  $S_Z$  parametrization it is possible to investigate the kinematics of the motion along the Z track. The simplest measures, are the velocity and speed of motion. The velocity,  $V_Z(i)$  at time  $T(i)$ , was defined as

$$V_Z(i) = [S_Z(i+1) - S_Z(i-1)]/[T(i+1) - T(i-1)]$$

where  $S_Z(i)$  is the position at time  $T(i)$ .

We calculated the velocities as a function of  $S_Z$  on two time scales: 96 sec ( $3 \times 32$  sec position points) and 588 sec ( $3 \times 196$  sec). We found, as did Hertz *et al.* (1992), that the range of possible velocities, and the variance in the velocities, increased up the FB. In addition, a similar, but much

less well-pronounced trend was found in the 96sec measurements as Sco X-1 moved on the NB. However, away from the FB, on a time scale of 588sec the variance in  $V_Z$  is indistinguishable from a monotonic function of  $S_Z$ , being lowest in the HB and highest in the FB. These trends in  $V_Z$  were found to exist at the 95% confidence level using Bartlett's test for many variances (Walpole and Myers 1978). The distribution in velocities was symmetric about zero. Specifically, on the FB this means that during flares the time spent on the rise and fall are on average the same.

The velocity can therefore be meaningfully recast as the speed along the Z track. The speed is defined as the absolute value of the velocity; it has no information about the direction of motion along the Z track. Fig. 14 is a plot of the average speed versus position. It can be clearly seen that on 96sec time scales Sco X-1 moves most slowly just before the NB/FB vertex, i.e., where the NBO frequency is between 7 and 8Hz. As the source moves through the vertex into the FB the average speed increases rapidly. Thus one expects that also the N/FBO frequency changes more rapidly in time on the FB. This accords with the rates at which the QPO frequency was found to change near the vertex: slowly on the NB side and much faster on the FB. The average speed increases along the flaring branch which could indicate that larger flares are steeper (higher amplitude but similar duration) or the flares are convex in shape.

The acceleration

$$A_Z(i) = [V_Z(i+1) - V_Z(i-1)]/[T(i+1) - T(i-1)]$$

was also found to have a larger scatter in the FB than in the HB-NB. No meaningful correlations were found between acceleration and position or velocity.

A direct search was made for hysteresis in the dependence of power spectral shape on velocity. Each observation was split into separate  $S_Z$  ranges. Power spectra were sorted according to the sign of the velocity. Two weighted average power spectra were formed; one where the velocity was positive and the other where it was negative. The average powers in a number of frequency ranges (0.01–1 Hz, 1–10 Hz, 10–20 Hz, 20–40 Hz, 40–60 Hz) were compared using the Student's t-test with unequal variances. The variances of the powers in each frequency range are unequal because there are generally slightly different numbers of positive and negative velocity power spectra. In all cases sufficient power spectra were averaged so that the average powers were very close to being normally distributed. In two cases there was a significant (95% confidence) difference in average power within the 10–20 Hz frequency band. Both cases were near the NB/FB vertex. This is just where hysteresis could be accommodated given the increased scatter in QPO frequencies near the vertex. However, there is a more mundane explanation. Since, near the vertex, the QPO frequency depends sensitively upon the position, any difference in the distribution of  $S_Z$  values corresponding to the positive and negative velocity power spectra will lead to different average QPO shapes. This explanation was tested as follows.

There were different numbers of individual power spectra averaged together in the positive/negative velocity average power spectra. The average spectrum with the greater number was recalculated but with some individual spectra removed, such that number of individual power spectra in each average spectrum was made equal. Either the individual power spectra corresponding to the highest speeds or those corresponding to the lowest speeds were removed. In either case (more positive or more negative velocities), for all  $S_Z$  regions, the statistical tests now showed no significant difference between the positive and negative velocity average power spectra. In addition all pairs of original average power spectra were fitted with a VLFN + HFN components and where necessary LFN or Gaussian peak(s). The fit parameters for all pairs of power spectra were the same within their 2  $\sigma$  errors. Our conclusion is that there is no evidence for hysteresis in the power spectra.

We made another search for hysteresis by testing if Sco X-1 took different paths on the CD depending on whether it was traveling up or down a branch. In several  $S_Z$  ranges spanning the Z track we tested if there was a difference in the average deviation from the smooth Z track ( $D_Z$ ) depending on whether the velocity was positive or negative. We found no significant difference (95% confidence) in the average  $D_Z$  in any  $S_Z$  range.

#### 4: Discussion.



We have presented a comprehensive description of the variation, as a function of Z-track position  $S_Z$ , of all power spectral components of Sco X-1. The Z-track position is considered to be a measure of the mass transfer rate onto the compact object for reasons outlined in the introduction. All the power spectral properties are found to vary in a systematic, but not always smooth fashion with  $S_Z$ . The QPO frequency and the HFN cut-off frequency change abruptly at the normal/flaring branch vertex. Here we compare our results with those found for other sources and with the current theoretical understanding of QPO.

For any comparison between Z sources one must bear several limitations in mind. Three other sources, namely GX 5-1 (Lewin *et al.* 1992, Kuulkers *et al.* 1994), GX 17+2 (Kuulkers *et al.* 1996) and GX 340 (Kuulkers & van der Klis 1996), have now been examined in sufficient detail to accurately characterize the variations in all power spectral parameters as a function of  $S_Z$ . Cyg X-2 is the best characterized of the other Z sources. A direct comparison of our results can be made with those of Kuulkers *et al.* (1994, 1997) because of the common definition of  $S_Z$ . We shall also compare our results with those of Hasinger *et al.* (1990) for Cyg X-2 and Lewin *et al.* (1992) for GX 5-1, in which a slightly different scaling was used, in that the lowest observed count rate end of the HB was fixed at rank=0, the HB/NB vertex at 1 and the lowest brightness point observed on the NB, as opposed to the NB/FB vertex, was fixed at rank=2. The thus defined “rank number” is therefore not scaled by the length of the NB as is  $S_Z$ . A direct comparison of  $S_Z$  with rank number can only be reliably made on and near the NB; otherwise only general trends with position can be compared. Some earlier studies of other Z-sources can be recast in terms of  $S_Z$  because the power spectra are sorted according to their place upon a CD or HID. This is the case for the studies of GX 340+0 by Penninx *et al.* (1991) and to a lesser extent GX 17+2 by Penninx *et al.* (1990).

A similar situation exists when trying to compare our results with other studies of Sco X-1. The concept of using an arc length to measure the position along the Z track originated with Hertz *et al.* (1992). Their parameter  $s_z$  is an arc length along the Z track with the NB/FB as the zero point. It is specific to the colours used. However, we can make valid comparisons with the Hertz *et al.* work because of the good coverage of the FB. We can fix, approximately, three points that are at the same position of the Z track and so approximately rescale the arc lengths of Hertz *et al.* to our  $S_Z$  parameter. The three calibration points are: the NB/FB vertex, the position at the top of the flaring branch (assuming both studies cover the entire FB) and the point where the FBO become undetectable.

Other complications are that various authors have used different functional forms to represent the power spectral components and different integration ranges for measuring the strength of the broad band noise components. The strengths of all components have a strong energy dependence, so there are also differences in measured amplitudes depending upon the energy band and detector used. There are also differences in the way in which various authors take into account deadtime and background.

Bearing in mind these comments we will give a summary of our results and a comparison with similar results for Sco X-1 and other Z-sources.

#### 4.1: VLFN.

It has been suggested (van der Klis 1991) that the VLFN is due to the motion of the source along the Z track. This idea is consistent with the spectral calculations of Psaltis *et al.* (1996). The similarity we find in the behaviour as a function of  $S_Z$ , of the VLFN amplitude and the average speed of motion along the Z track, supports this contention. Both are approximately constant along the HB-NB and then increase rapidly along the FB. It is possible to quantitatively test this hypothesis by comparing the rms variability spectrum of the VLFN and the slope of the Z track at the same  $S_Z$  on either a hardness-intensity diagram or a colour-colour diagram. In a CD with soft colour  $C_S$  and hard colour  $C_H$ , we can consider two colour-colour points  $(I_2/I_1, I_4/I_3)$  and  $((I_2 + a_2)/(I_1 + a_1), (I_4 + a_4)/(I_3 + a_3))$  as being representative of the effect of the VLFN on the colours and calculate the expected slope of the branch if the VLFN is indeed motion along the branch. Here the  $I_i$ 's and  $a_i$ 's are the background subtracted count rates and the rms variability amplitude of the VLFN in the  $i$ th energy band. Given that the *fractional* rms amplitude  $r_i \equiv a_i/I_i$ , the expected slope  $\theta_{VLFN}$  of a branch due to VLFN variability is:

$$\theta_{VLFN} = \frac{(I_4 + a_4)/(I_3 + a_3) - I_4/I_3}{(I_2 + a_2)/(I_1 + a_1) - I_2/I_1} = \frac{I_4/I_3 (r_4 - r_3) (1 + r_1)}{I_2/I_1 (r_2 - r_1) (1 + r_3)},$$

which should be identical with the measured slope  $\theta_{CD}$  on the colour-colour diagram:

$$Z - \text{track slope} = \theta_{CD} = \frac{\Delta C_H}{\Delta C_S}.$$

As  $r_1$  and  $r_3$  are generally  $\ll 1$  we can approximate the factor on the right in the expression for  $\theta_{VLFN}$  with unity and express the above identity in terms of the relative slopes  $\beta_{VLFN}$  and  $\beta_{CD}$ :

$$\text{Relative variability slope} = \beta_{VLFN} \cong \frac{r_4 - r_3}{r_2 - r_1} \equiv \theta_{CD} = \frac{\Delta C_H / \overline{C}_H}{\Delta C_S / \overline{C}_S} = \beta_{CD}$$

We are able to test the equality of the Z-track relative slope  $\beta_{CD}$  and the expected relative slope due to VLFN variability ( $\beta_{VLFN}$ ) for two points on the flaring branch; at the mid FB and the top of the FB (points E and F in Fig 1). Only at these points were we able to measure the VLFN rms amplitude in all energy bands. At other places on the Z track there is not enough signal to measure the VLFN in the lowest energy band. In both positions on the FB we find that the measurements are consistent (90% confidence) with the VLFN being solely due to motion along the Z track. However, the errors are large enough to encompass a factor of 1.5 difference between the measured Z track relative slope ( $\beta_{CD}$ ) and  $\beta_{VLFN}$ .

If the VLFN is solely a product of motion along the Z track then we expect that within each branch the power spectra of  $S_Z$  to be a scaled version of the VLFN component in the power spectra of count rate. This is because the relation between  $S_Z$  and count rate is approximately linear (Fig. 3). Although we cannot, with the present data, measure the power spectrum of  $S_Z$  on time scales on which the VLFN is typically observed, i.e.,  $< 200$  sec, we can measure the count rate power spectra on longer time scales and compare them to the  $S_Z$  power spectra.

Fourier transforms of the  $S_Z$  values were performed using the fast implementation of the Lomb-Scargle method for unequally spaced data (Press *et al.* 1992 and references therein). No data windowing was applied. Each data set was taken individually. In each  $S_Z$  power spectrum an unbroken power law component was found. The  $S_Z$  power law index ranged from 1.3 to 2.2 with no discernible trend with respect to branch. The average index was  $1.7 \pm 0.05$ , similar to that of the VLFN found on shorter (128 sec) time scales.

We have made a direct comparison between the power spectra of count rate and  $S_Z$  for two data sets; one on the NB (11-12 March 1986) and one mostly on the FB (Aug 24 1985). The long (4096 sec) count rate power spectra (Fig. 15 top panels) show that the power law form of the VLFN component is unbroken out to time scales of more than 1000 sec. Working from the other direction, the power spectra of  $S_Z$  show an unbroken power law on time scales from about a 9 hours down to a few hundred seconds (Fig. 15 bottom panels). The fitted (VLFN+HFN model) power law slopes of the VLFN component in the count rate power spectra from the NB and FB are  $1.51 \pm 0.04$  and  $1.76 \pm 0.03$  respectively over the range  $8 \times 10^{-4}$  to 0.2 Hz. For the  $S_Z$  power spectra the power law slopes measured over the  $\sim 0.01$  to  $3 \times 10^{-5}$  Hz range are  $1.65 \pm 0.25$  and  $1.50 \pm 0.20$  at on the normal ( $\overline{S_Z}=1.2$ ) and flaring ( $\overline{S_Z}=2.2$ ) branches. So, the power law indices of the count rate power spectra and the  $S_Z$  power spectra are consistent with one another on both branches and also consistent with the  $\alpha_{VLFN}$  at the same positions as plotted on Fig. 5. Since we have measured similar power indices in two sets of power spectra, spanning frequency ranges that overlap from  $\sim 0.1$  to  $\sim 10^{-3}$  Hz we conclude that it is likely that we are dealing with the same phenomenon, i.e., motion along the Z track. A similar inference is drawn from the results of Scargle *et al.* (1993) who have shown, using wavelet analysis and a scalegram that the VLFN extends, remaining approximately self-similar and hence being described by a constant slope power law (Scargle *et al.* 1993), from time scales of about 16 sec to at least 9 hours. Note that Scargle *et al.* used an observation (25 Feb 1985) covering both the NB and FB.

We combined data from consecutive days to produce  $S_z$  power spectra extending to time scales near a day using data taken on 11-13 March 1986 (mostly NB plus a little HB) and 24-25 Aug 1985 (mostly FB). In the case of the March 1986 data (the longest and most complete data set) we found an unbroken power law slope with  $\alpha=1.3\pm0.1$ , over the range  $2\times10^{-5}$  to  $\sim0.01$  Hz., i.e., between time scales of 10sec and nearly 14 hours. This slope is in the range of the power law indices of the VLFN on the upper NB/HB ( $\alpha=1.1-1.5$ , see Fig. 5.). The 1985 data set is more disjointed than that of 1986 and so suffers more from windowing. The slope was found to be  $1.4\pm0.05$  over the span  $4\times10^{-5}$  ( $\sim7$  hours) to  $2\times10^{-2}$  (50 sec). This slope is lower than the average slope ( $1.7\pm0.05$ ) of the VLFN on the FB.

Thus the power law shape of the power spectrum of  $S_z$  extends unbroken to at least a 14 hours time-scale with no sign of a turn-over. The power spectrum must turn-over at some point. The long term behaviour of Sco X-1 is known to consist of periods of flaring activity lasting 2-3 days separated by periods of about 10 days of quieter activity, i.e., the NB/HB. This pattern became evident from numerous monitoring campaigns; the most recent being with BATSE (McNamara *et al.* 1993) and the RXTE/ASM. Thus the turnover time-scale is likely to be several days.

Recently, three alternative models dealing specifically with the VLFN have been proposed. All three rely on self organized criticality to explain the power law slope of the VLFN. The classic example of a system that exhibits a self organized critical (SOC) state is an idealized pile of sand. As more and more sand is added, the pile will reach a point when the addition of even a single grain will set off an avalanche which returns the pile to below the critical state. SOC models have been applied to a wide range of natural phenomena. Their main strength is that they naturally produce power-law power spectra for a wide range of parameters.

Bildsten (1995) has proposed that the VLFN in Z and atoll sources can be identified with unsteady nuclear burning on the neutron star's surface. This is a self organized critical system (Bildsten, 1995, *private communication*). Two relevant observational consequences of this model are that the burning luminosity ( $L_B$ ) is expected to scale with  $\dot{M}$  and the power law index increases with accretion rate. Thus, the overall behaviour of the VLFN can be explained by this model. However, there are observations that it fails to explain. The power spectrum computed by Bildsten is not a power law but has a characteristic timescale in contrast to our observation the the VLFN power spectrum which is well represented by a power law over a wide range of timescales. Also, the energy output of nuclear burning is of course limited. Matter falling onto a neutron star releases about 100 MeV per proton. Hydrogen burning produces 4 MeV/proton while helium burning alone yields 0.9 MeV/proton and other fusion reactions up to iron can yield a further 6 MeV/proton. Therefore, being optimistic, up to 11% of the accretion luminosity can be released by nuclear burning. The high (up to  $25\pm4\%$  rms. See Fig. 5) VLFN amplitude seen on the upper FB strains the model. What fractional rms amplitude is measured as VLFN depends upon the the shape of the light curves from the individual nuclear burning events and their coherence (Bildsten 1995). However, these properties are severely constrained by the observed power law slope of the VLFN down to  $\sim1$  mHz. For example, more spiky wave-forms yield a higher fractional rms amplitude, but also a steeper power law slope at a higher turn-over frequency for the VLFN. One possible way out of these constraints is that the X-ray energy spectra of the nuclear and the accretion flux are different, with part of the accretion-generated flux below the observable X-ray energy range. This could also explain why the VLFN rms amplitude spectrum increases with energy while most of the flux from nuclear burning is expected at low energies. However, postulating different energy spectra is entirely ad-hoc. Another problem with the idea that the VLFN is due to nuclear burning is that it dissociates motion through the Z track, and therefore  $\dot{M}$ , from the brightness variations comprising the VLFN. This means that on some time-scale small  $S_z$ -variation related brightness changes must merge "invisibly" into the VLFN brightness changes so that the power spectrum does not show a break.

In a model for the power law component of BHC power spectra which may also be applicable to the VLFN, Mineshige *et al.* (1994a) cited the variability in the accretion disk. Their approach was to consider the accretion process through a disk as a self organized critical (SOC) process. Initial simulations produced a power law index of 1.8 which is similar to the power law index of the VLFN of AGN and Z-sources. Further simulations (Mineshige *et al.* 1994b, Takeuchi *et al.* 1995) including diffusion, i.e., the gradual motion of the material inward through the disk, reduced

the power index to values as low as  $\sim 1.1$ . The power law slope also depends upon the inclination of the disk (Abramowicz & Bao 1994). So far, there is no indication of how the amplitude of the variations or the power law index depends upon average  $\dot{M}$ .

The “dripping handrail” model for the VLFN and QPO, by Scargle *et al.* (1993), and Young and Scargle (1996) is very similar in concept to that of Mineshige *et al.*. Their simulations were able to reproduce not only the VLFN shape but also can produce QPO whose frequency corresponds to the refill time-scale of the inner disk. The frequency of the model QPO was proportional to accretion rate which does not seem to fit the observations.

#### 4.2: HFN.

We have detected HFN in all branches for Sco X-1, smoothly decreasing in strength (Xe band: 5–18 keV) from 7.5% rms in the HB, to 6.3% rms at the NB/FB vertex, and then to 5.5% rms (Xe band) at the end of the FB. Hertz *et al.* (1992) also found a decrease in HFN strength along the FB; from  $5.4 \pm 0.4\%$  rms (5.8–15.7 keV) near the NB/FB vertex to  $1.6 \pm 0.1\%$  rms in the upper FB. The difference in measured strength can be attributed mostly to the difference in the energy responses of the EXOSAT ME and Ginga LAC instruments. Other Z-sources also show a decrease in HFN strength as the source moves from the HB to the FB (Hasinger & van der Klis 1989). The EXOSAT instrumental broad band component makes only a small contribution because it is compensated by our slight overestimate of the Poisson noise level in the power spectra (see Sect. 2.3 for a full discussion). Because of these instrumental uncertainties one must be cautious in interpreting HFN amplitudes and frequency extents measured using EXOSAT.

The HFN was weaker in rms variability by a factor of  $\sim 0.5$  in the Ar energy band (1–15 keV) than in the Xe band (5–18 keV). A similar strong energy dependence was found by Hertz *et al.* (1992) where the HFN was, roughly, twice as strong in the hard (5.8–15.7 keV) band as in the soft (1.2–5.8 keV) band. So far, the energy dependence of the HFN has not been measured in any other Z-source.

Because of its weakness and the uncertainties in deadtime correction the HFN has in other Z-source analyses always been assumed to have  $\alpha_{HFN}=0$ . We could measure this quantity for Sco X-1. The average power law slope was slightly positive ( $0.066 \pm 0.001$ ) which indicates an on average “red noise” shape. There is only slight evidence for a change of slope with  $S_Z$ . The slope is higher ( $0.071 \pm 0.012$ ) in HB & NB and ( $0.02 \pm 0.04$ ) on the FB.

We find evidence that the HFN cut-off frequency is affected by the NB/FB transition. Near this vertex it undergoes a drop from  $\sim 75$  Hz to  $\sim 35$  Hz for  $\alpha_{HFN}=0$ . This drop occurs within a span of  $< 0.3$  in  $S_Z$ . We have no information on its timewise behaviour near the NB/FB vertex. In both the HB-NB and FB the cut-off frequency appears to increase with  $S_Z$ . No other Z source has sufficient count rate with EXOSAT or Ginga to measure the  $S_Z$  dependence of the HFN cut-off frequency.

#### 4.3: LFN.

In the HB, the LFN has an amplitude (0.001–1 Hz) of  $2.8 \pm 0.2\%$  rms and a slope  $\alpha = -1.55 \pm 0.48$ . Soon after entering the normal branch the LFN amplitude decreases, becoming undetectable ( $0.4\%$ ,  $2\sigma$  upper limit) at  $S_Z=1.4$ . At the HB/NB vertex the power law index increases rapidly while the cut-off frequency increases to  $> 8$  Hz. This represents a change in shape; the LFN becomes broader.

We find that the LFN is stronger at higher energies. Similar hard spectra for the LFN have been found from GX 340+0 (Penninx *et al.* 1991) and GX 5-1 (Lewin *et al.* 1992).

The shape (peaked or red) of the LFN is one of several characteristics that seem to split the Z-sources into two groups. Sco X-1 and GX 17+2 have “peaked” LFN while in Cyg X-2, GX 5-1 and GX 340+0 the LFN is a “red” noise component (Hasinger and van der Klis 1989, Penninx *et al.* 1990 & 1991, and Kuulkers *et al.* 1994, 1996, 1997). Inclination as well as neutron star magnetic field strength have been suggested as the underlying difference between the two groups. Kuulkers *et al.* 1994, 1996 discuss the inclination idea and give evidence for two groups. Psaltis, Lamb & Miller,

(1995) discuss the magnetic field hypothesis. The detailed behaviour of the LFN, as a function of  $S_z$ , may not follow this division of sources. For Cyg X-2 (high inclination group) there is a small rise in LFN amplitude just before entering the NB (Fig. 9 of Hasinger 1991). However, for GX 5-1, which is of the same group, the LFN amplitude decreases monotonically (Kuulkers *et al.* 1994 and Lewin *et al.* 1992). In GX 340+0 the LFN also amplitude decreases monotonically (Kuulkers & van der Klis 1996) while for GX 17+2 there are insufficient HFN measurements (Kuulkers *et al.* 1996) to tell one way or the other. Also for Sco X-1 we cannot tell, because of the large errors associated with the fits, whether the LFN rms amplitude reaches a local maximum, as a function of  $S_z$ , in the HB.

#### 4.4: HBO.

No HBO were found in this study of Sco X-1. An upper limit of 3.1% rms (90% confidence, Xe band: 5–18 keV) is set. This limit is set by the strongest candidate power spectral peak found in the HB data. This peak was near 35 Hz with no evidence for an brightness dependence in its frequency. In the cases of GX 5-1 and Cyg X-2 the HBO and LFN are similar in amplitude (rms ratio = 0.75–1.0) at all energies between 1 and 10 keV. If this holds for Sco X-1, we expect to see HBO with an amplitude near 2–3% rms (ie comparable with our measured LFN amplitude). Our upper limit is consistent with this estimate. In fact, the HBO of GX 17+2, the Z-source most similar to Sco X-1 has relatively weak HBO, i.e., the HBO/LFN amplitude ratio is  $\sim 0.5$  (Hasinger and van der Klis 1989, confirmed by Kuulkers *et al.*, 1996). If this ratio holds for Sco X-1 then we expect the HBO to have an amplitude of only  $\sim 1.5\%$  rms. Thus, it is not surprising that HBO has not been detected from Sco X-1 during the only known HB observation.

A HBO-like feature has recently been discovered in the NB of Sco X-1 (van der Klis *et al.* 1997) with a frequency near 45 Hz, FWHM of 15–55 Hz and an rms amplitude  $\sim 1\%$ . This feature is in line with the above amplitude limits.

#### 4.5: NBO/FBO.

The rms amplitude of the Sco X-1 N/FBO increases steadily along the NB-FB till it is too broad to be distinguished from the HFN and Poisson noise. GX 17+2, the only other source where both the NBO and FBO have been observed shows the frequency and amplitude higher in the FB than in the NB. The QPO at the vertex is near 7–8 Hz (Pennix *et al.* 1990). For GX 5-1, there is a strong increase in NBO strength, but no noticeable increase in frequency with  $S_z$ . (Lewin *et al.* 1992, Kuulkers *et al.* 1994). Cyg X-2 shows an increase in NBO frequency from 5.5 to near 7 Hz in the lower FB but the strength remains constant or even decreases (Hasinger 1993, *private communication*). For GX 340+0 the NBO amplitude and frequency are constant within the large (1.5% rms and 1 Hz) scatter. It seems that different sources behave differently as a function of  $\dot{M}$ . The fact that these differences do not correlate with the sub-grouping of Z-sources indicates that not all timing differences are governed by one single parameter such as inclination (Kuulkers *et al.* 1994, 1996) or magnetic field strength (Psaltis, Lamb & Miller 1995).

It has been suggested that the NBO are the result of a radiation-force/opacity feed-back loop within a spherical flow region (Lamb 1989). Alternatives are sound waves in a thick disk (Alpar *et al.* 1992) or g-mode oscillations in the neutron star (Bildsten & Cutler 1995, Bildsten *et al.* 1996).

There are concerns about how to excite a single g-mode oscillation at the neutron star's surface with sufficient amplitude to be detectable <sup>1</sup>. The main observable difference between g-mode oscillations and other models is that when a second harmonic is excited it should have a frequency a factor  $\sqrt{3}$  rather than a factor of two greater than the fundamental. The frequency change across the NB/FB vertex provides a potential discriminator. However, our data is consistent with either model.

We will now concentrate on the interpretation of our observations in terms of the radiation-force feedback model. The spherical flow region (Lamb 1989) is expected to become prominent only

<sup>1</sup>Bildsten *et al.* 1996 show that g-modes can only be sustained in slowly rotating neutron stars which seems unlikely given the identification of  $\approx 360$  Hz burst QPO's with neutron star spin frequencies.

above  $\sim 0.8L_{Edd}$ . At luminosities  $\geq L_{Edd}$  the smooth flow will be broken up by “bubbles” of photons being pushed out by buoyancy. At some point any oscillation modes will be destroyed. The NB/FB vertex is thought to occur within a few percent of the Eddington limit.

This scenario nicely explains the limited extent over which the QPO are visible. We find QPO from Sco X-1 over only 17% of the Z track in the lowest third of the NB and the lowest 10% of the FB measured in terms of  $S_Z$ . The  $S_Z$  positions at which the QPO first become measurable are practically the same between sources; i.e., for Sco X-1:  $S_Z=1.5$ , GX 5-1:  $S_Z=1.5$  (Kuulkers *et al.* 1994), Cyg X-2: rank=1.6 or  $S_Z=1.3$  (Hasinger, 1993, *private communication*, GX 17+2:  $S_Z=1.4-1.5$  (Kuulkers *et al.* 1997) and for GX 340+0:  $S_Z=1.2$  (Kuulkers & van der Klis 1996). The FBO of GX 17+2 are limited to about the lowest 15% of the FB (Penninx *et al.* 1990).

At the high luminosities observed from Z-sources radiation forces increase the dynamical time-scale of the inward material flow. The fastest time-scale seen for the 7 Hz to >12 Hz transition was  $\leq 90$  sec. Although this is the fastest time-scale reported for the change in NB/FBO frequency it is still much longer than the estimated dynamical time-scale of  $\approx 1$  sec (Lamb 1989), and so cannot constrain models.

The most remarkable result presented here is the rapid change with respect to both  $S_Z$  and time in NB-FB QPO frequency at the NB/FB vertex. The frequency-position diagram shows that the QPO frequency is very sensitive to position near the vertex.

This sensitivity to Z-track position has not been previously noted. The frequency-intensity diagram used by Priedhorsky *et al.* (1986) emphasizes the smooth continuous nature of the transition but not its restricted range upon the Z track. With hindsight, Fig. 7 of van der Klis *et al.* (1987) also shows a jump in QPO frequency near the NB/FB vertex from near 7 Hz to 12 Hz. Here the QPO frequency is plotted against the black body luminosity ( $L_{BB}$ ) as determined from two component fits to the X-ray energy spectrum. Both  $L_{BB}$  and  $S_Z$  are postulated to be directly related to the mass accretion rate onto the neutron star. The sense of the change in QPO frequency with  $L_{BB}$  is the same as with  $S_Z$ . The range in  $L_{BB}$  over which the QPO frequency changed from 6.5 to 12 Hz occurred is only  $\sim 13\%$  of the range in which QPO were measurable. This is similar to the  $\leq 8\%$  range in  $S_Z$ .

The jump in N/FBO frequency at the NB/FB vertex can be viewed as the result of either a sensitive dependence of frequency upon the underlying controlling parameter, presumably  $\dot{M}$  (but see the next paragraph), with  $S_Z$  approximately proportional to this controlling parameter. An alternative view is that the relationship between  $S_Z$  and  $\dot{M}$  is different near the NB/FB vertex, with a proportionally larger change in  $\dot{M}$  as Sco X-1 moves the short distance around the vertex as compared to motion in other places on the Z track. Either way, the NB/FB vertex represents a critically important Z-track position.

Within the context of a unified model of the flow about low mass neutron stars (Lamb 1989), modeling of the Z track (Psaltis, Lamb & Miller, 1995) suggests that  $\dot{M}$  changes smoothly along the Z track. Thus in this model the sensitivity of QPO frequency on  $S_Z$  is not due to changes in the relation between  $S_Z$  and  $\dot{M}$ . The parameter controlling the behaviour of the flow onto the neutron star is the difference between the accretion rate and the Eddington critical rate. The radial flow region becomes prominent only when the luminosity is within 20% of  $L_{Edd}$ . Much closer (within 2%) to the Eddington accretion rate the flow conditions are expected to become more complex. The initial model for the N/FB QPO of Fortner, Lamb and Miller (1989) considered only radial ( $\ell=1$   $n=1$ ) oscillations in a smooth spherical inflow region at luminosities not too close to  $L_{Edd}$ . This model successfully accounts for the observed low frequency of the QPO and in the case of Cyg X-2 the dependence of the NBO amplitude and relative phasing with energy (Miller & Lamb, 1992 and references therein). If the outer radius of the cool flow is constant the model predicts that the NB/FBO frequency decreases with increasing mass flux in contrast to our observations. However the behaviour of the outer radius is difficult to model and hence uncertain. Recently Miller & Park (1995) have considered non-radial oscillations within the inflow region. At accretion rates  $\sim 0.8$  to  $0.98 L_{Edd}$  any non-radial modes are well damped. But as the luminosity increases to within 2% of  $L_{Edd}$  they find that the higher frequency non-radial modes (e.g.  $\ell=1$ ,  $n>1$  or  $\ell=2$ ,  $n>1$ ) are much less damped and can dominate the lower order oscillations and so the frequency

risers. The span in luminosity over which the higher frequency modes begin to dominate is very similar to the range in  $S_Z$  over which the NB/FBO oscillations increase in frequency. These higher order modes continue to be excited as the source exceeds the Eddington limit but will be suppressed as the flow becomes fragmented. In this picture, the anomalous frequency excursions we observe may be the result of momentary switches between oscillation modes.

#### 4.6: Is $\dot{M}$ all there is?

Although direct searches for hysteresis failed we have found two indications that position along the Z track is not the only parameter governing the behaviour of Sco X-1. First the minimum values of count rate reached during NB/FB transitions are variable on time scales of several thousand seconds. This behaviour would contribute to the increased scatter of intensities and QPO frequency seen in the lowest parts of the NB and FB as seen on a frequency-intensity diagram. Secondly; the two anomalous frequency excursions that clearly break the paradigm of a one-to-one relation between spectral state as determined from position in a colour-colour diagram and timing properties.

The common features of these cases are that they occur at or near the NB/FB vertex (i.e.  $L_{Edd}$ ) and that their time scales are short. There thus may be a link with the changes in the flow expected near  $L_{Edd}$ . The exact nature of the flow and the resulting QPO could depend upon other factors in addition to  $\dot{M}$ . For example, which of the QPO modes dominates may depend upon the optical depth of the flow as Sco X-1 reaches  $L_{Edd}$ . Observationally, the way to proceed is to examine the X-ray spectral, QPO and noise properties on shorter time scales than was possible with our data, especially near the NB/FB transition where we have shown that the QPO properties are particularly sensitive to the underlying controlling parameters.

## Acknowledgments.

We gratefully acknowledge many useful discussions with Erik Kuulkers, Brian Vaughan, Lars Bildsten, Fred Lamb and Guy Miller. This work was supported by the Netherlands Organization for Scientific Research (NWO) under grant PGS 78-277 and S.D. was also partially supported by grant ERB-CHRX-CT93-0329 of the European Commission (HCM program).

## References.

- Alpar M.A., & Shaham J., (1985) *Nature*, **316**, 239.
- Alpar M.A., Hasinger G., Shaham J., Yancopoulos S., (1992) *Astron. Astrophys.*, **257**, 627.
- Ambramowicz M., & Bao G., (1994) *Publ. Astron. Soc. Japan* **46**, 523.
- Augusteijn T., Karatasos K., Papadakis M., Paterakis G., Kikuchi S., Brosch N., Leibowitz E., Hertz P., Mitsuda K., Dotani T., Lewin W.H.G., van der Klis M. & van Paradijs J., (1992) *Astron. Astrophys.*, **265**, 177.
- Andrews D., & Stella L., (1985) *EXOSAT Express*, **10**, 35.
- Berger M., & van der Klis M., (1994) *Astron. & Astrophys.*, **292**, 175.
- Berger M., & van der Klis M., (1998) *Astron. & Astrophys.*, *Astron. & Astrophys.*, bf 340, 143.
- Bildsten L., (1995), *Astrophys. J.*, **438**, 852.
- Bildsten L., & Cutler C., (1995) *Astrophys. J.*, **449**, 800.
- Bildsten L., Ushomirsky G., & Cutler C., (1996), *Astrophys. J.*, **460**, 827.
- Deeter J.E., (1984) *Astrophys. J.*, **281**, 482.

- Fortner B., Lamb F.K., & Miller G.S., (1989) *Nature*, **342**, 775.
- Giacconi R., Gursky H., Paolini F., & Rossi B., (1962) *Phys. Rev. Lett.*, **9**, 439.
- Haberl F., (1992) *Legacy*, **1**, 53.
- Hasinger G., (1987a) *Astron. Astrophys.*, **186**, 153.
- Hasinger G., (1987b) in *The Origin and Evolution of Neutron Stars*, D.J. Helfand & J.-H. Haug (eds.) IAU Symp. 125, p333.
- Hasinger G., (1991) in *Particle Acceleration near Accreting Compact Objects*, J. van Paradijs, M. van der Klis, & A. Achterberg (eds.) Royal Netherlands Academy of Arts and Sciences., North Holland, Amsterdam, p23.
- Hasinger G., Langmeier A., Sztajno M., Trümper J., Lewin W.H.G., & White N.E., (1986), *Nature*, **319**, 469.
- Hasinger G., Priedhorsky W.C., & Middleditch J., (1989) *Astrophys. J.*, **337**, 843. (HPM89).
- Hasinger G. & van der Klis M., (1989) *Astron. Astrophys.*, **225**, 79. (HK89).
- Hasinger G., van der Klis M., Ebisawa K., Dotani T. & Mitsuda K., (1990) *Astron. Astrophys.*, **235**, 131.
- Hertz P., Vaughan B., Wood K.S., Norris J.P., Mitsuda K., Michelson P.F., & Dotani T., (1992) *Astrophys. J.*, **396**, 201.
- Hjellming R.M., Stewart R.T., White G.L., Strom R., Lewin W.H.G., Hertz P., Wood K.S., Norris J.P., Mitsuda K., Penninx W., & Paradijs J., (1990) *Astrophys. J.*, **365**, 681.
- Jain A., Hasinger G., Pietsch W., Proctor R., Reppin C., Trümper J., Voges W., Kendziorra E., & Staubert R., (1984) *Astron. Astrophys.*, **140**, 179.
- Kuulkers E., van der Klis M., Oosterbroek T., Asai K., Dotani T., van Paradijs J., & Lewin W.H.G., (1994), *Astron. Astrophys.*, **289**, 795. Erratum (1995) *Astron. Astrophys.*, **295**, 842.
- Kuulkers E., (1995) Ph.D. Thesis, *EXOSAT observations of Z Sources*, University of Amsterdam.
- Kuulkers E., van der Klis M., (1995) *Astron. Astrophys.*, **303**, 801.
- Kuulkers E., van der Klis M., & van Paradijs J., (1995) *Astrophys. J.*, **450**, 748.
- Kuulkers E., & van der Klis M., (1996) *Astron. Astrophys.*, **314**, 567.
- Kuulkers E., van der Klis M., & Vaughan B.A., (1996) *Astron. Astrophys.* **311**, 197.
- Kuulkers E., van der Klis M., Oosterbroek T., van Paradijs J., & Lewin W.H.G., (1997), *Mon. Not. Roy. Astron. Soc.*, **287**, 495.
- Lamb F.K. (1989) in *Proc. 23rd ESLAB Symp. in Two Topics in X-ray Astronomy*, J. Hunt & B. Battrick (eds.), ESA SP-296, **Vol. 1** p215.
- Lamb F.K., Shibazaki N., Alpar M.A., & Shaham J., (1985) *Nature*, **317**, 681.
- LaSala J., & Thorstensen J.R., (1985) *Astron. J.*, **90**, 2077.
- Langmeier A., Hasinger G., & Trümper J., (1990) *Astron. Astrophys.*, **228**, 89.
- Leahy D.A., Darbro W., Elsner R.F., Weisskopf M.C., Sutherland F.G., Kahn S., & Grindlay J.E., (1983) *Astrophys. J.*, **266**, 160.
- Lewin W.H.G., van Paradijs J., & van der Klis M., (1988) *Spa. Sci. Rev.*, **46**, 273.



- Lewin W.H.G., Lubin L.M., Tan J., van der Klis M., van Paradijs J., Penninx W., Dotani T., & Mitsuda K., (1992) *Mon. Not. Roy. Astron. Soc.*, **256**, 545.
- McNamara B., Fitzgibbons G., Fishman G.J., Meegan C.A., Wilson R.B., Harmon B.A., Paciesas W.S., Rubin B.C., & Finger M.H., (1994). *Compton Gamma-ray Observatory*, St Louis 1993, M. Friedlander, N. Gehrels & D.J. Macomb (eds.), AIP Press, New York, p391.
- Middleditch J., & Friedhorsky W.C., (1986) *Astrophys. J.*, **306**, 230.
- Miller G.S., & Lamb F.K., (1992) *Astrophys. J.*, **388**, 541.
- Miller G.S., & Park M-G., (1995) *Astrophys. J.*, **440**, 771.
- Mineshige S., Ouchi B., & Nishimori H., (1994a) *Publ. Astron. Soc. Japan*, **46**, 97.
- Mineshige S., Takeuchi M., & Nishimori H., (1994b) *Astrophys. J.*, **435**, L125.
- Mook D.E., Messina R.J., Hiltner W.A., Belian R., Conner J., Evans W.D., Strong I., Blanco V.M., Hesser J.E., Kunkel W.E., Lasker B.M., Golson J.C., Pel J., Stokes N.R., Osawa K., Ichimura K., & Tomita K., (1975) *Astrophys. J.*, **197**, 425.
- Penninx W., Lewin W.H.G., Mitsuda K., van der Klis M., van Paradijs J., & Zijlstra A.A., (1990) *Mon. Not. Roy. Astron. Soc.*, **243**, 114.
- Penninx W., Lewin W.H.G., Tan J., Mitsuda K., van der Klis M., & van Paradijs J., (1991) *Mon. Not. Roy. Astron. Soc.*, **249**, 113.
- Petro L.D., Bradt H.V., Kelley R.L., Horne K., & Gomer R., (1981) *Astrophys. J.*, **251**, L7.
- Pollock A.M.T., Carswell R.F., & Ponman T.J., (1986) poster presented at the workshop on *The Physics of Compact Objects* held in Tenerife, Spain.
- Ponman T.J., Cooke B.A., & Stella L., (1988) *Mon. Not. Roy. Astron. Soc.*, **231**, 999.
- Press W.H., Teukolsky S.A., Vetterling W.T., & Flannery B.P., (1992) in *Numerical Recipes: The Art of Scientific Computing* 2nd Edition. Cambridge University Press. Cambridge.
- Priedhorsky W., Hasinger G., Lewin W.H.G., Middleditch J., Parmar A., Stella L., & White N., (1986) *Astrophys. J.*, **306**, L91.
- Prins S., & van der Klis M., (1997) *Astron. Astrophys.*, **319**, 498.
- Psaltis D., Lamb F.K., & Miller G.S., (1995) *Astrophys. J.*, **545**, L137.
- Scargle J.D., Steiman-Cameron T., Young K., Donoho D.L., Crutchfield J.P., & Imamura J., (1993) *Astrophys. J.*, **411**, L91.
- Sztajno M., van Paradijs J., & van der Klis M., Langmeier A., Trümper J., & Pietsch W., (1986) *Mon. Not. Roy. Astron. Soc.*, **222**, 499.
- Takeuchi M., Mineshige S., & Negoro H., (1995) *Publ. Astron. Soc. Japan*. **47**, 617.
- Turner M.J.L., Smith A., & Zimmermann H.U., (1981) *Spa. Sci. Rev.*, **30**, 513.
- Ubertini P., Bazzano A., Cocchi M., La Padula C., & Sood R.K., (1992) *Astrophys. J.*, **386**, 710.
- van der Klis M., Jansen F., van Paradijs J., Lewin W.H.G., van den Heuvel E.P.J., Trümper J.E. & Sztajno M., (1985) *Nature*, **316**, 225.
- van der Klis M., Stella L., White N., Jansen F., & Parmar A.N., (1987) *Astrophys. J.*, **316**, 411.
- van der Klis M., (1989a) *Ann. Rev. Astron. Astrophys.*, **27**, 517.

- van der Klis M., (1989b) in *Timing Neutron Stars*, H. Ögelman & E.P.J. van den Heuvel (eds.), Kluwer, Dordrecht, NATO ASI Series C **262**, p27.
- van der Klis M., (1991) in *Neutron Stars: Theory and Observation*, J. Ventura & D. Pines (eds.), Kluwer, Dordrecht, NATO ASI Series C **344**, p319.
- van der Klis M., (1995a) in *Lives of Neutron Stars* Alpar M.A, Kiziloğlu Ü., & van Paradijs J.,eds. Kluwer, Dordrecht, NATO ASI Series C **450**, p301.
- van der Klis M., (1995b) in *X-ray Binaries*, W.H.G Lewin, J. van Paradijs & E.P.J. van den Heuvel (eds.) Cambridge, U.K., Astrophysics Series **26**, p252.
- van der Klis M., (1998) in *The Many Faces of Neutron Stars*, R. Bucccheri, J. van Paradijs, M.A. Alpar, Kluwer, Dordrecht, NATO ASI Series. (astro-ph/9710016).
- van der Klis M., Wijnands R.A.D., Horne K., & Chen W., (1997) *Astrophys. J.*, **481**, L97.
- Vaughan B.A., van der Klis M., Wood K.S., Norris J.P., Hertz P., Michelson P.F., van Paradijs J., Lewin W.H.G., Mitsuda K., & Penninx W. (1994) *Astrophys. J.* **435**, 362.
- Vrtilek S.D., Raymond J.C., Garcia M.R., Verbunt F., Hasinger G., & Kürster M., (1990) *Astron. Astrophys.*, **235**, 162.
- Vrtilek S.D., Penninx W., Raymond J.C., Verbunt F., Hertz P., Wood K., Lewin W.H.G., & Mitsuda K., (1991) *Astrophys. J.*, **376**, 278.
- Walpole R.E., & Myers R.H., (1978) in *Probability and Statistics for Engineers and Scientists* (2nd ed.) Macmillain Pub. Co., New York.
- White N.E., Peacock A., (1988) in *X-ray Astronomy with EXOSAT*, R. Pallavicini, & N.E. White (eds.), Mem. S. A. It. **59**, 7.
- Young K., Scargle J.D., (1996) *Astrophys. J.*, **468**, 617.

Table 1: Observation Log

Date and Day Number		Start Time (UT)	End Time (UT)	Dur. (sec)	Binning (ms)		Branch	Ref
					Time <sup>x</sup>	Energy <sup>y</sup>		
Observations examined in detail.								
29/30 Aug 1983	241/2	23:09	18:47	70720	8	2500 <sup>a</sup>	FB & NB <sup>h</sup>	1
03 Aug 1984	216	06:38	12:03	19328	8 <sup>c</sup>	312.5 <sup>b</sup>	NB→FB	2
25 Feb 1985	56	03:58	13:18	32104	2	—	NB→FB	3
24 Aug 1985	236	09:02	14:50	5784	4	4	FB	4
25 Aug 1985	237	13:05	20:18	25976	4	4	NB→FB	4
11/12 Mar 1986	70/71	16:37	11:05	66536	1	8	NB→HB	5
13 Mar 1986	72	02:18	12:03	35160	1	8	mid NB	5
”	72	16:13	19:03	10200	8 <sup>d</sup>	4	low NB	5
”	72-73	19:09	01:12	21716	1	8	low NB	5
Other data searched for frequency excursions. <sup>g</sup>								
11 Mar 1984	71	02:06	07:37	17224	8+125 <sup>e</sup>	5000 <sup>a</sup>	FB	1
13 Mar 1984	73	00:59	04:36	12800	8+125 <sup>e</sup>	5000 <sup>a</sup>	mid NB	1
26 Aug 1985	238	10:00	14:34	15696	4	4 <sup>f</sup>	NB	4
27 Aug 1985	239	04:19	14:16	34328	4	4 <sup>f</sup>	FB→NB	4

x Unless otherwise noted all high time resolution data is taken with the HTR3 or HTR5 OBC modes, using solely the Xe filled chambers. Only the fastest available sampling is listed.

y Unless otherwise stated this column refers to HER7 data with energy boundaries at 0.9, 3.1, 4.9, 6.6 and 19.5 keV. Only the fastest available sampling is listed.

<sup>a</sup> Multichannel data; affected by overflows.

<sup>b</sup> Multichannel HER5 data.

<sup>c</sup> Ar+Xe combined count rate.

<sup>d</sup> Various combinations of the HTR5 and HER7 modes were used.

<sup>e</sup> Four sets of single channel data (one from each pair of Xe detectors) at 125 ms time resolution in addition to the count rate sum every 8 ms from all Xe detectors. The corresponding energy resolved data (5000 ms) is from the Ar and Xe detectors of each half array separately.

<sup>f</sup> Four energy channel data (HER7) but with 2 Ar channels and 2 Xe channels.

<sup>g</sup> Observations on 7/8 Aug 1983 were also examined, but no QPO were found. However, the time resolution and continuity were generally inadequate to detect QPO.

<sup>h</sup> The FB→NB transition occurs during a gap in the data.

[1] van der Klis *et al.* (1987)

[2] Pollock *et al.* (1986)

[3] Middleditch & Priedhorsky (1986)

[4] Priedhorsky *et al.* (1986)

[5] Hasinger, Priedhorsky & Middleditch (1989)

Table 2: Energy dependence of power spectral components

	Sz	VLFN		LFN		QPO		HFN	
		%rms (0.001–1Hz)		%rms (0.001–100Hz)				%rms (1–500Hz)	
		Ar	Xe	Ar	Xe	Ar	Xe	Ar	Xe
A	0.645±0.075	0.9 ± 0.1	1.0 ± 0.1	1.9 ± 0.2	3.7 ± 0.25			3.0 ± 0.45	6.8 ± 0.3
B	1.473±0.075	0.46 ± 0.05	1.6 <sup>+0.13</sup> <sub>-0.09</sub>		1.8 <sup>+1.3</sup> <sub>-0.2</sub>			4.0 ± 0.1	7.0 ± 0.1
C	1.735±0.040	0.8 ± 0.4	2.5 ± 0.07			1.3 ± 0.08	3.3 ± 0.15	4.2 ± 0.1	6.4 ± 0.2
D	2.161±0.072	1.8 ± 0.1	3.1 <sup>+0.3</sup> <sub>-0.2</sub>			<2.12 (1 $\sigma$ )	6.5 <sup>+0.4</sup> <sub>-0.2</sub>	2.57 ± 0.65	5.55 ± 0.35
E	2.753±0.151	3.9 ± 0.2	6.9 <sup>+0.9</sup> <sub>-0.7</sub>	1.15 ± 0.7	3.0 <sup>+0.7</sup> <sub>-0.3</sub>			2.41 ± 0.75	5.5 <sup>+0.3</sup> <sub>-0.4</sub>
F	4.108±0.301	9.3 <sup>+2.7</sup> <sub>-1.7</sub>	23.0 <sup>+4.4</sup> <sub>-2.9</sub>					4.1 ± 0.7	5.25 <sup>+1.4</sup> <sub>-0.5</sub>

The amplitudes for the Ar data were found by fixing all other parameters to the values from the Xe fits. Full fits to the Ar and Xe power spectra showed that all non-amplitude parameters were the same within  $<2\sigma$ . However, the errors were much larger for the Ar power spectra.

The "LFN" of spectrum E is an extra QPO/LFN like component at  $\simeq 5.5$  Hz.

**Fig. 1.** The colour-colour diagram of Sco X-1 showing the complete Z-track. The data were gathered using the HER7 mode, which gives data in 4 energy channels. The integration time is 196 sec per point. Typical errors are shown at three different places in the Z-track. The horizontal, normal and flaring branches are labeled as HB, NB and FB, respectively. The solid curve is the Z-track representation used to calculate  $S_z$  and  $D_z$  (see text). It is marked off at intervals of 0.5 in the values of  $S_z$ . The frequency of the QPO is given at 4 places along the Z-track. Higher on the Z-track than the points marked “6 Hz”, and “20 Hz” the QPO are not detectable. Also labeled, as A,B,C,D,E,F, are the positions at which the 6 representative power spectra of Fig. 4 were taken.

**Fig. 2.** The colour-colour diagram based upon the HER5 mode data taken on 3 Aug 1984. The colour-colour points were calculated in the same energy bands as in Fig. 1. The solid curve is the Z-track representation of the 3 Aug 1984 data. The dash-dotted curve is the Z-track from Fig. 1. The differences in Z-track position and orientation are within the uncertainties in the colours caused by uncertainties in the background and changes in the gain of the Ar counters.

**Fig. 3.** The Xe count rate (background subtracted and scaled to 8 detectors) versus Z-track position ( $S_z$ ). The individual data points correspond to intervals in time or  $S_z$  where power spectra were calculated. Near the NB/FB vertex ( $S_z=2$ ) linear fits were made between count rate and position. The slope on the NB side of the vertex is  $-2120 \pm 70$  cts/ $S_z$ -unit and on the FB side  $1500 \pm 200$  cts/ $S_z$ -unit. The count rate at the vertex is  $2239 \pm 26$  cts/sec/8 detectors.

**Fig. 4.** Representative power spectra. The expected Poisson level has been subtracted and corrections have been made for the effects of differential deadtime. The errors are 1 sigma. The positions on the Z-track where these spectra were taken are shown on Fig. 1. At each position two spectra are shown; one from the 2–20 keV Ar data (open squares, lighter smooth curve) and the other from the 5–35 keV Xe data (filled circles, bolder smooth curve). The smooth curves represent the best fits to the power spectra. In Fig. 4C, two fits are given for the Ar data; one with the HFN cut-off frequency fixed at that derived from the Xe data and the other with the cut-off frequency as a free parameter. In Fig. 4E, there are also two fits for the Ar power spectrum, i.e., with and without an extra peaked noise component that is required to fit the Xe data.

**Fig. 5.** The parameters of all broad band noise components as a function of Z-track position ( $S_z$ ). The HB/NB vertex at  $S_z=1$  and the NB/FB vertex at  $S_z=2$  are marked by dotted vertical lines. Each point was derived from a fit to an average of a number of power spectra obtained at the  $S_z$  value shown. Each individual power spectrum was calculated from 128 sec of Xe band (5–50 keV) timing data. The fit always included VLFN and HFN components and, if required, either a LFN or a QPO component. The error bars in  $S_z$  show the span covered during each fit. The vertical error bars represent the  $1\sigma$  single-parameter errors as determined from a scan in  $\chi^2$  space. The rms amplitudes were corrected for differential deadtime effects.

**Fig. 6.** The relative width of the QPO (FWHM/QPO frequency) as a function of  $S_z$ . The QPO are most coherent near  $S_z=1.75$ .

**Fig. 7.** The variation of QPO properties with Z-track position ( $S_z$ ). The same symbols as in Fig. 1 are used to identify data from different observations. Panels **a** and **b** show the fractional rms amplitudes (corrected for differential deadtime and frequency binning) for the Ar+Xe (HER5; 3 Aug 1984) and Xe only (HTR; 1985–86) data respectively. Note that the QPO is always weaker at lower energies. Panel **c** shows the QPO frequency. Here the Xe-only and the Ar+Xe data are shown together. The transition between the NB and FB is not resolved. It occurs within  $\pm 0.05$   $S_z$ -units of the NB/FB vertex. Panel **d** shows the frequency-intensity diagram. The count rates are for the Xe data with background subtraction and scaled to the full array of 8 detectors. In this panel there are extra points not present in the other panels. These points (represented by error bars only) are from 25 Feb 1985, when there was excellent timing, but no energy-resolved data. Two data points are circled in each panel. These points correspond to the 13 Mar 1986 anomalous excursion to higher QPO frequencies (see text).

**Fig. 8.** The detailed behaviour of Sco X-1 during the anomalous frequency excursion of 13 Mar 1986. Time is measured from 16:13 UT when the observation began. The time of highest QPO frequency and X-ray count rate is labeled “Peak”, the two count rate dips associated with 8 Hz QPO are labeled “Dip”. The top two panels show the measurements of the HER7 colours as used in the colour-colour diagram of Fig. 1 and used to calculate the values of  $S_z$ . The thick line represents the average colours over the same time intervals as used to measure the power spectra. This is the same binning as used in Figs. 7, 9 and 10. The thin line shows the colours as measured with a 32 sec integration time. The 3rd panel shows the values of  $S_z$  as calculated from these colours. The  $S_z$  values represented by the thick line are those calculated from the colours measured with a 16 sec integration time, averaged over the selected data

sections and processed using the correction/replacement algorithm described in Sect. 2.1. The thin line shows a  $3 \times 32$  sec point binning of the  $S_z$  values before any corrections were applied. Comparison of the two curves shows that the low  $S_z$  measurements at the time of the frequency excursion ( $1.510^4$  sec) do not result from our correction/replacement method. The 4th panel shows the Ar/Xe hardness ratio (colour). Whereas the individual HER7 colours do not show any clear changes this hardness ratio clearly shows dips at the times of the count rate dips. The 5th panel shows the variations in QPO frequency. The line represents measurements made by fitting the power spectra. One sigma errors are indicated. The points result from a completely different method for measuring the QPO frequency, where a threshold power level was set and the mode frequency of the powers above this threshold was found. The formal errors are of the order of 3–4 Hz when a 32 sec integration time is used. The bottom panel shows the Xe and Ar count rates as defined in Sect. 2.

**Fig. 9** The frequency-intensity diagram for Sco X-1, including the track taken during the frequency excursion on 13 Mar 1986. The shaded area shows the region covered by Sco X-1 during in all our observation (see Fig. 7). The position of the count rate/frequency peak (“Peak”) is marked, as well as the positions of the two count rate and colour dips (“1st Dip” and “2nd Dip”). The “Start” and “End” points of the frequency excursion are also indicated. These are points just preceding the first dip and following the second dip. Although the Peak and Dips are consistent with other data, Sco X-1 does not follow its usual track when moving to and from the peak.

**Fig. 10.** As Fig. 9, but with the colours instead of count rate. The shaded area shows the region usually occupied by Sco X-1. This area includes the  $1\sigma$  uncertainties on individual points of a normal NB/FB transition on 25 Aug 1985.

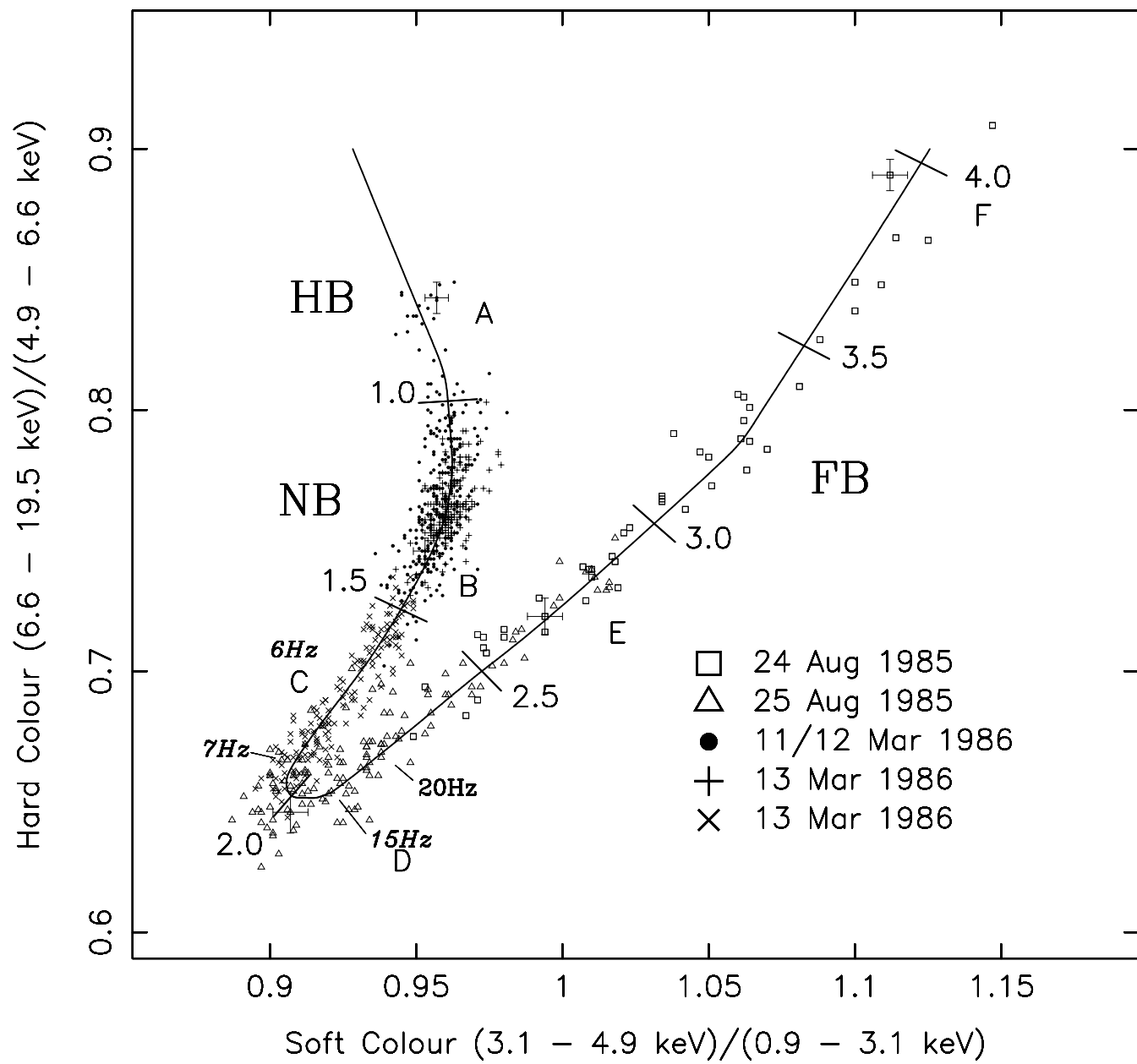
**Fig. 11.** An enlarged version of the colour-colour diagram of Fig. 1 showing the path Sco X-1 took during the 13 Mar 1986 anomalous frequency excursion. The data marked with the connected line covers exactly the same span and is integrated in exactly the same way as the data of Figs. 8,9 and 10. Three points are emphasized with filled symbols; the first count rate dip (circle), the count rate peak (triangle) and the second count rate dip (square). Note that Sco X-1 does *not* enter the flaring branch during the excursion.

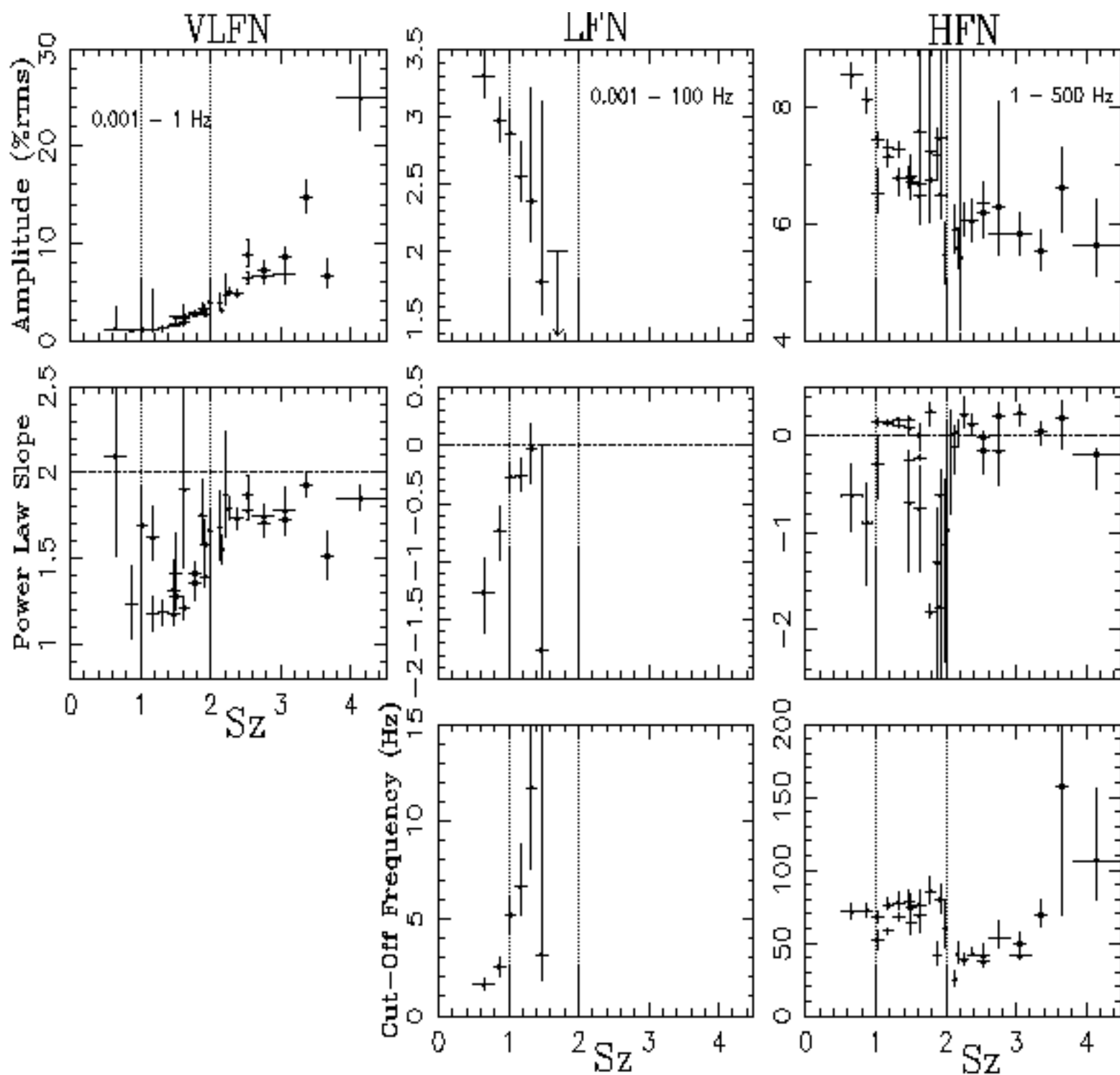
**Fig 12.** The detailed behaviour of Sco X-1 during the anomalous frequency excursion with “looping behaviour” on the 30 Aug 1983. Several times are marked. Ip is the time of the count rate peak, Fp is the time of the frequency peak and A and B are times when the count rate dips. The point where the frequency drops rapidly is labeled Jump. This jump is discussed in Sect. 3.5. The bottom panel shows the ME Xe detector and GSPC 2–8 keV band count rates. In both cases the background has been subtracted. EXOSAT’s pointing was unstable during the first 1500 sec of the observation, which started at 10:11 UT, but no corrections have been made for collimator response changes. The ME count rates have been scaled to the full 8-detector array. The middle panel shows the hardness ratio (HR) formed from the the ratio of the 8–15 keV and 2–8 keV GSPC counting rates. The thick curve represents the HR as measured on the same time intervals as used to average the power spectra. The thin line is the hardness ratio measured, using the GSPC with an 8 sec time resolution. The top panel shows the variation in QPO frequency. The curve follows the fits to the power spectra. The one sigma errors are from a scans in  $\chi^2$ . The points are frequency estimates made by finding the modal frequency of powers exceeding a preselected power level (see Fig. 9).

**Fig 13.** The frequency-colour diagram of the anomalous frequency excursion on 30 Aug 1983. There is a clear jump between frequencies typical of the flaring and normal branches. A frequency-intensity diagram also shows this.

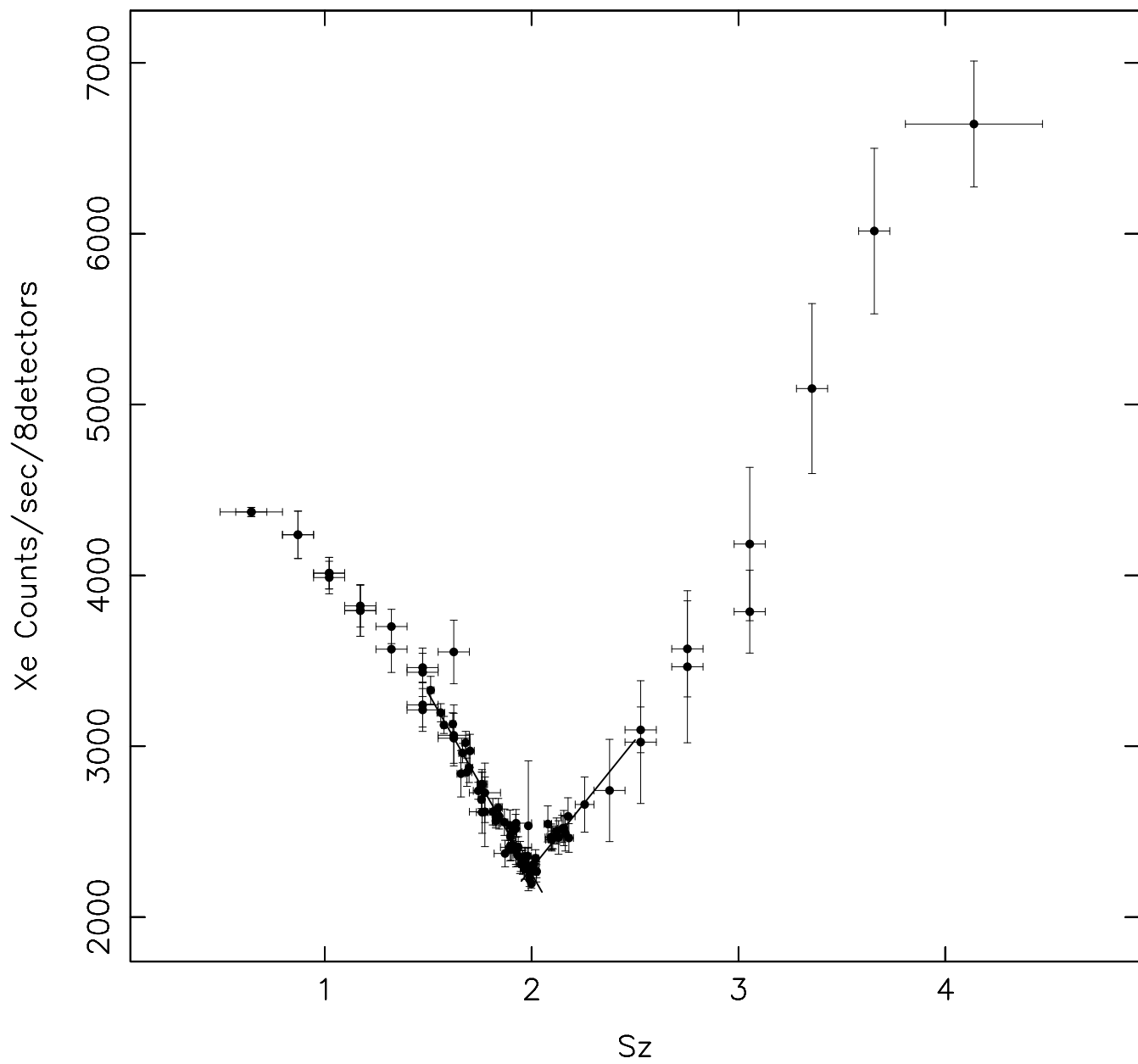
**Fig 14.** The average speed (arbitrary units) of the motion of Sco X-1 along the Z-track as a function of Z-track position ( $S_z$ ). On short (96 sec) time scales Sco X-1 moves slowest at the NB/FB vertex.

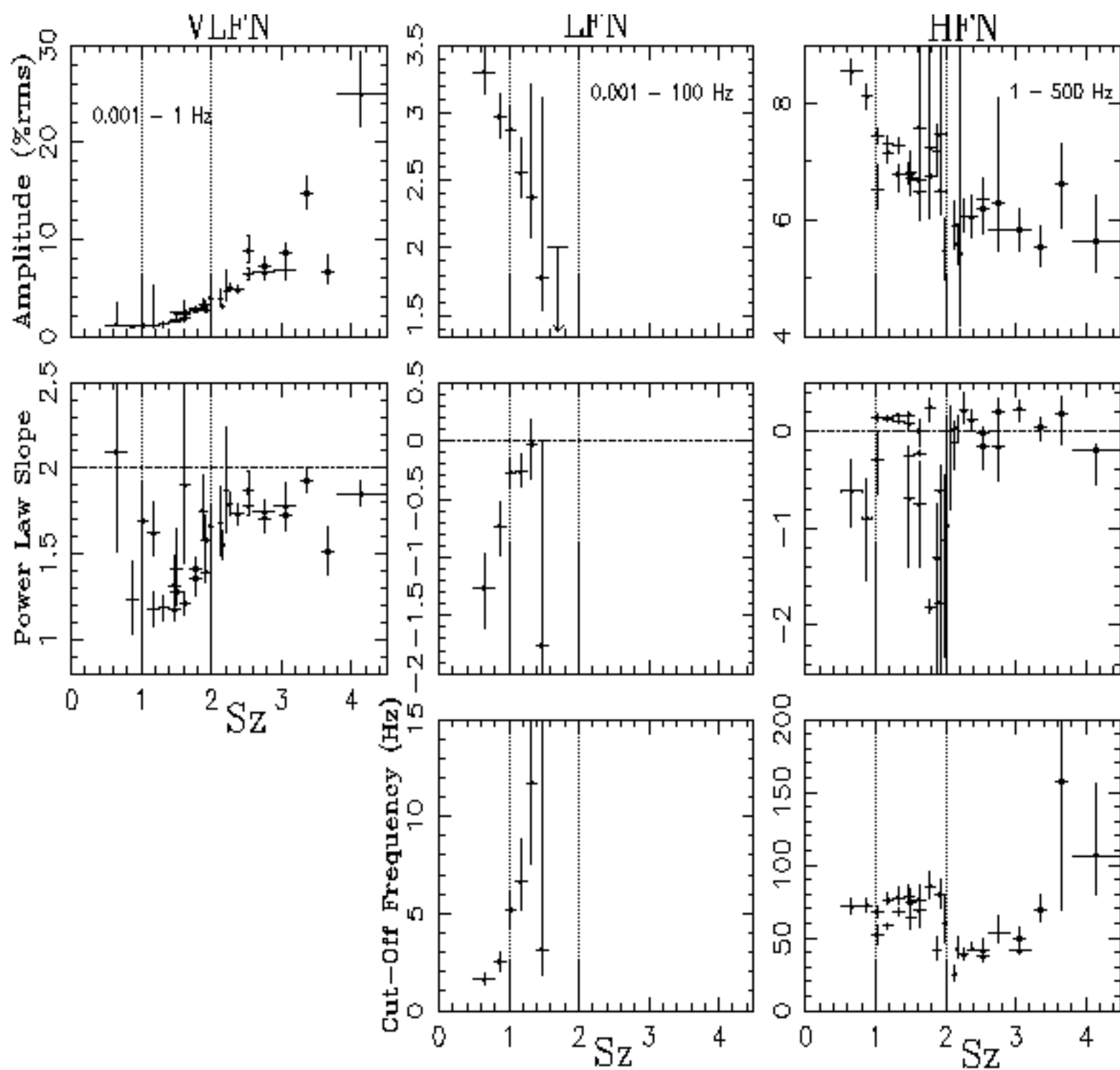
**Fig 15.** A comparison between count rate power spectra and  $S_z$  power spectra down to low frequencies. The top two panels show the count rate power spectra for the data taken on 11/12 March 1986 (left, mostly NB data) and 25 Aug 1985 data (right, mostly FB data). The lower two panels show the power spectra of the  $S_z$  values for the same observations, again 11/12 March 1986 on the left and 25 Aug 1985 on the right. The count rate power spectra are normalized in the same manner as the power spectra of Fig. 4. The expected Poisson level has been subtracted. The  $S_z$  power spectra were calculated using the fast implementation of the Lomb-Scargle periodogram for unevenly spaced data (Press *et al.* 1992 and references therein). The normalization is in terms of the data variance. The noise level, as estimated from the average power at the highest frequencies, has been subtracted.



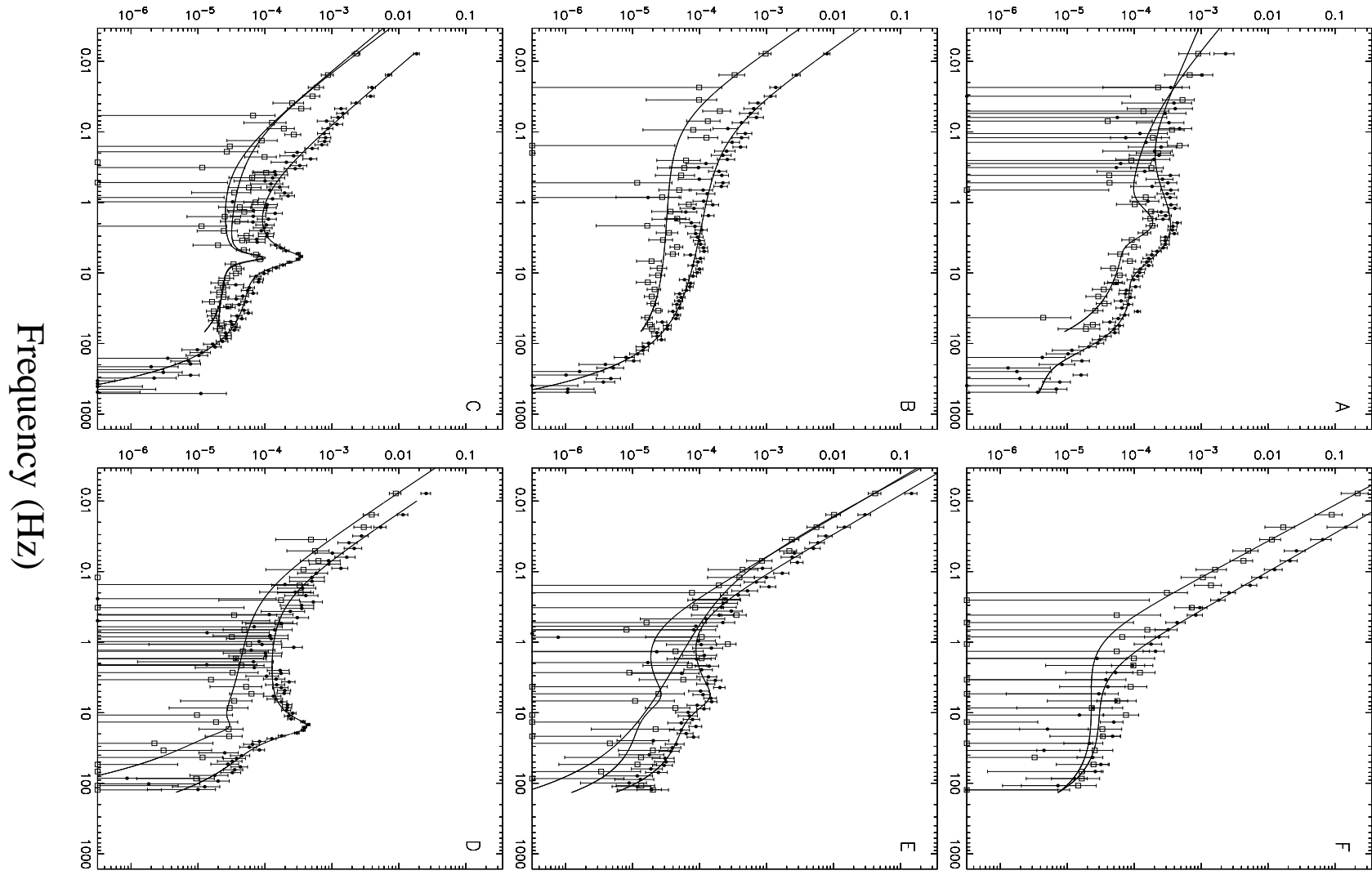


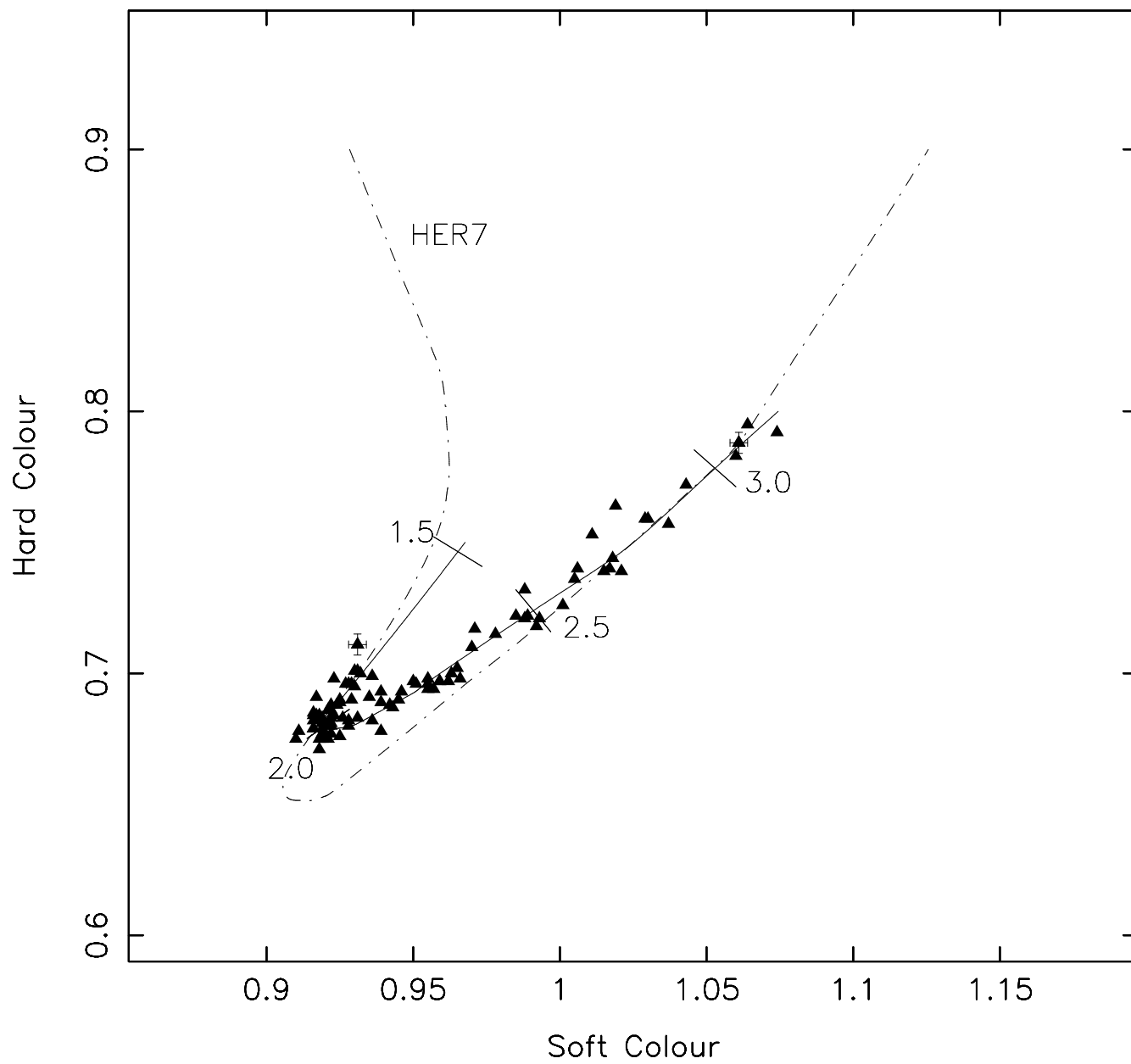


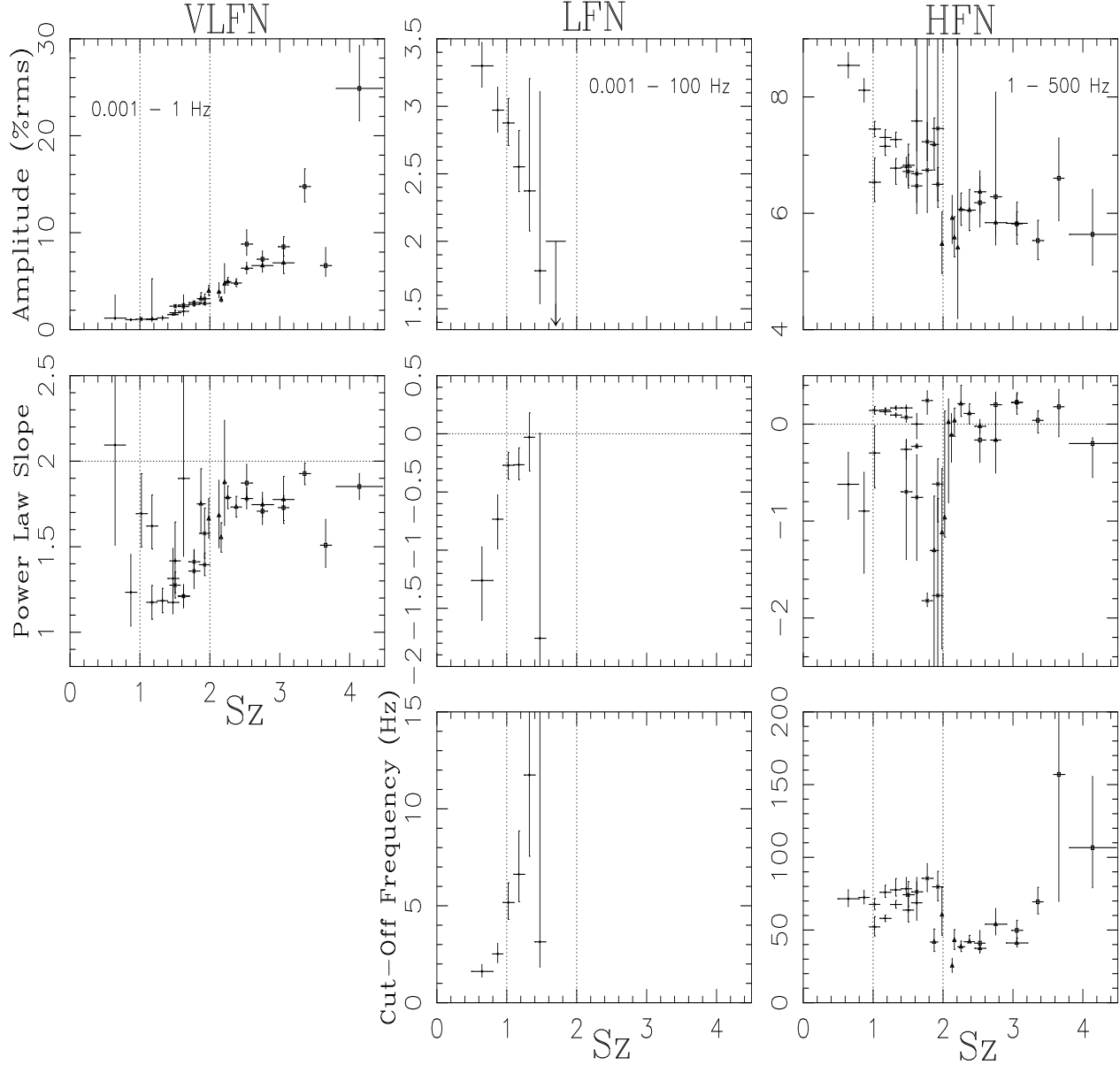


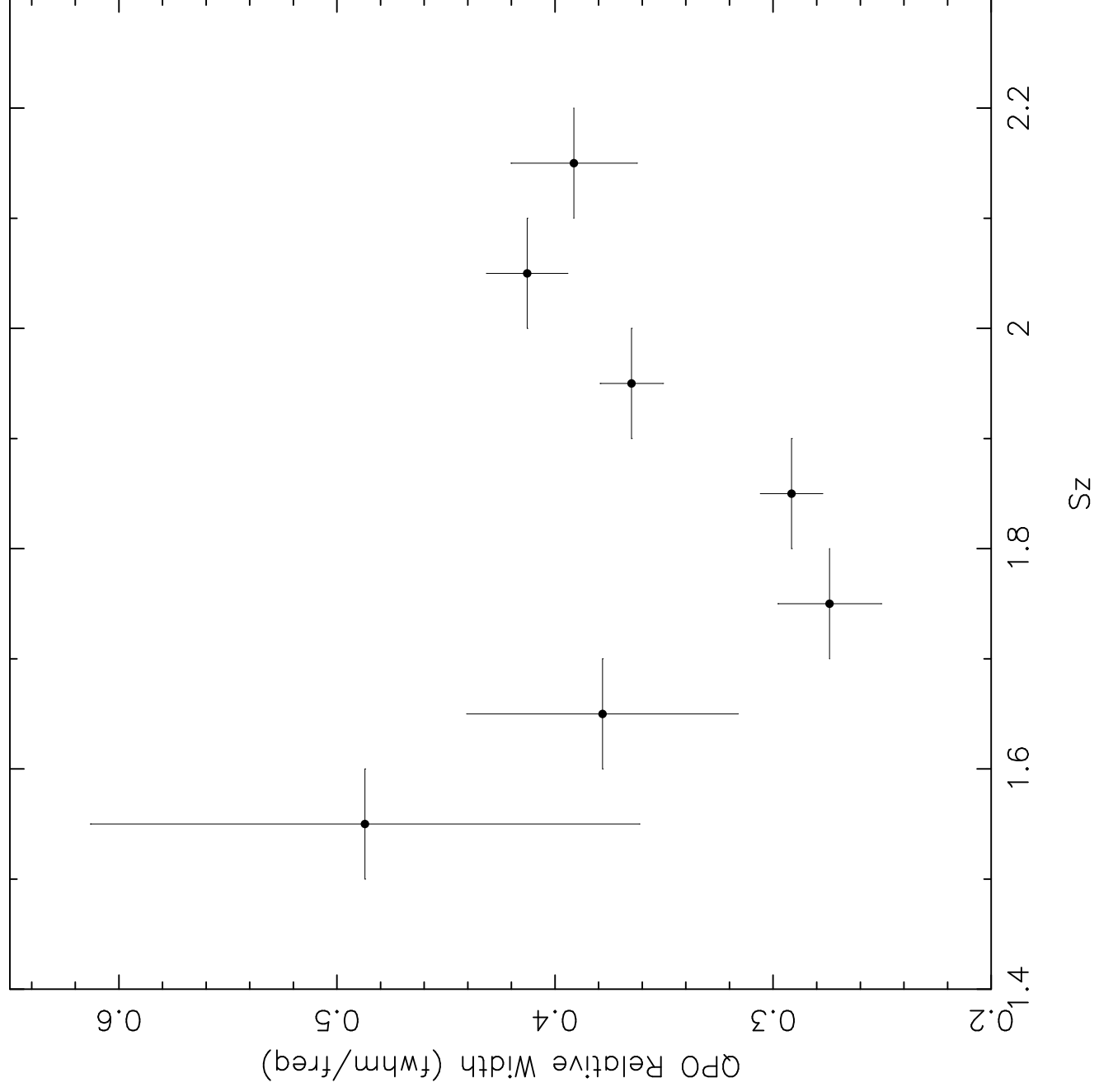


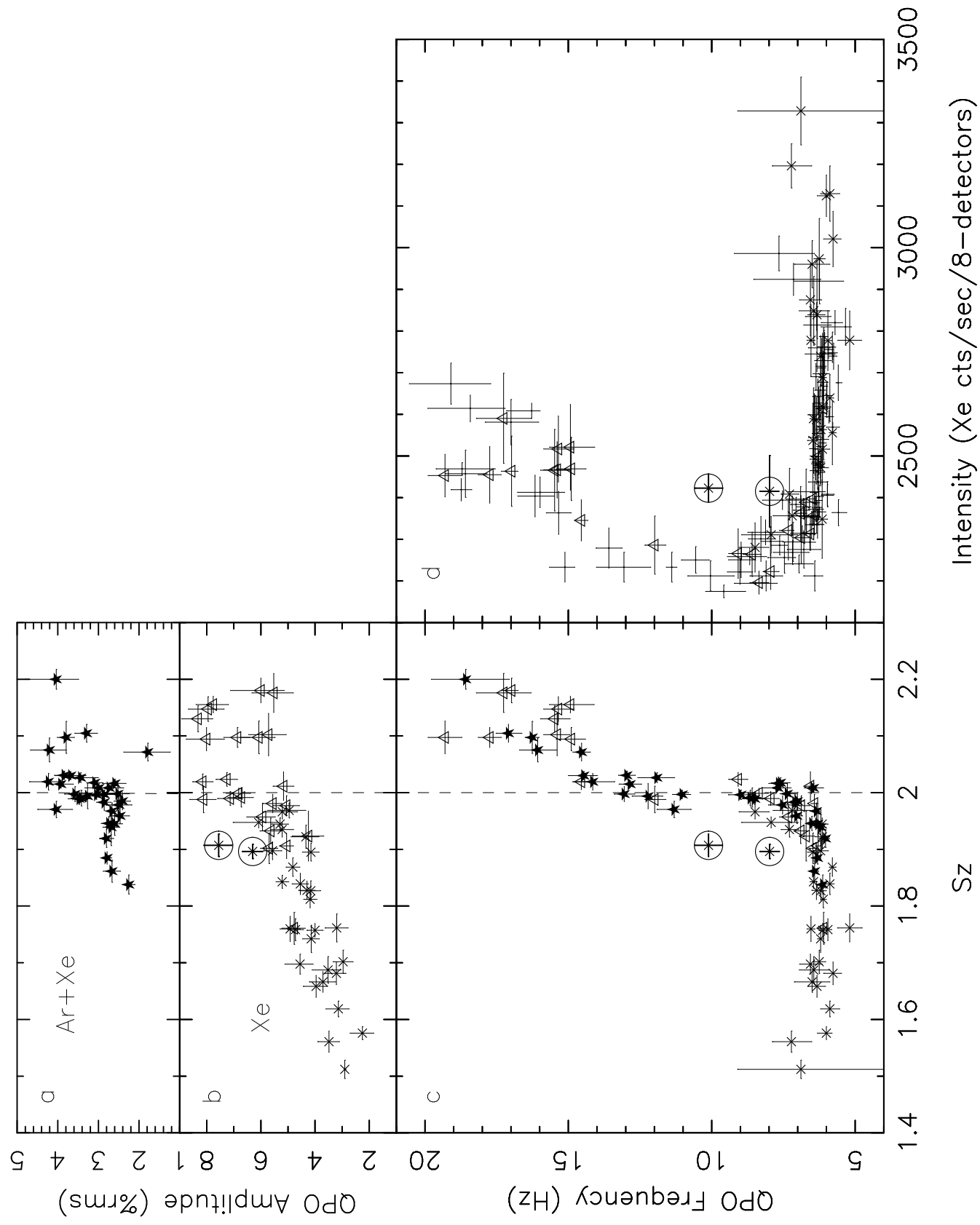
Power (RMS/mean)<sup>2</sup> Hz<sup>-1</sup>

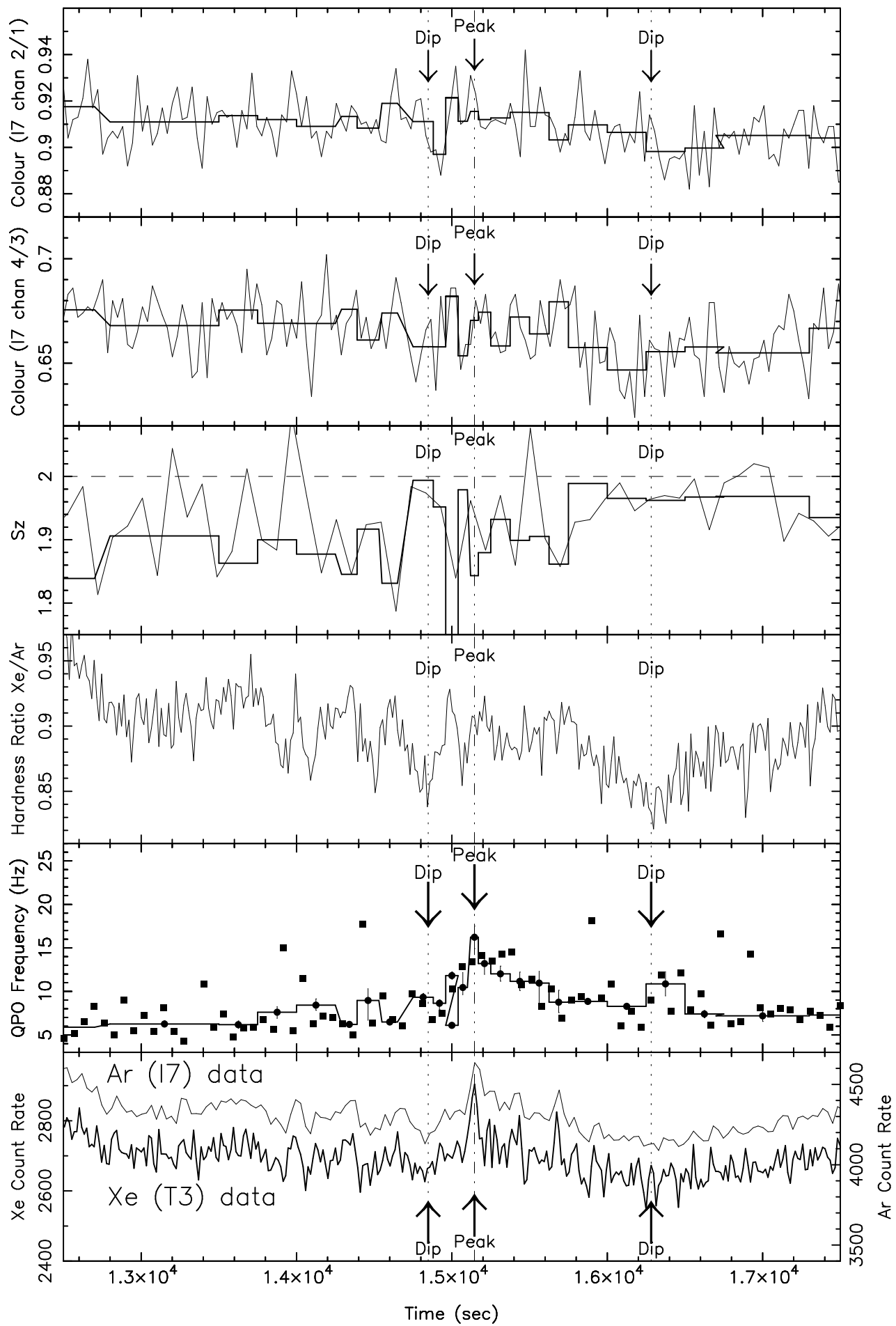




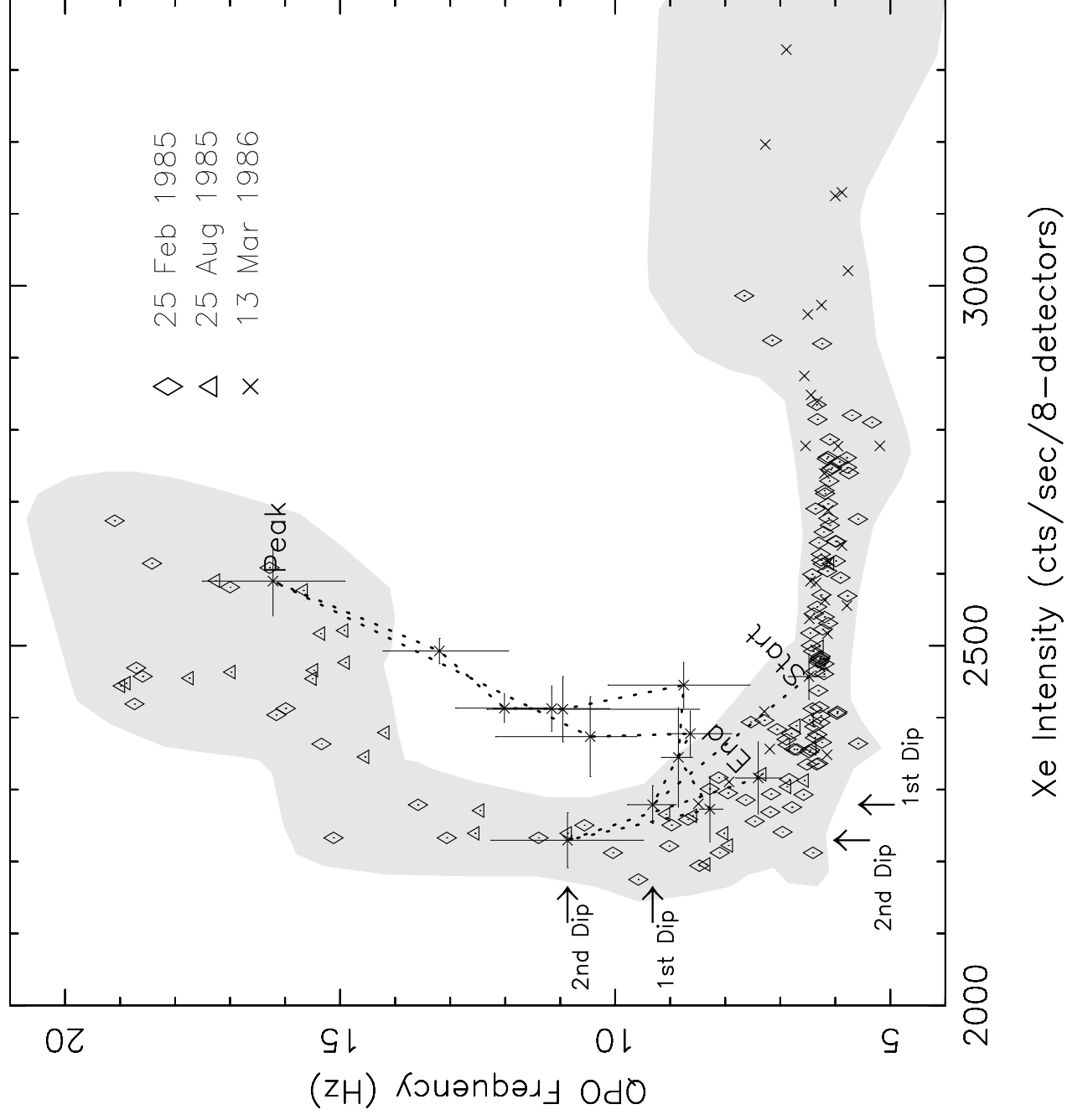


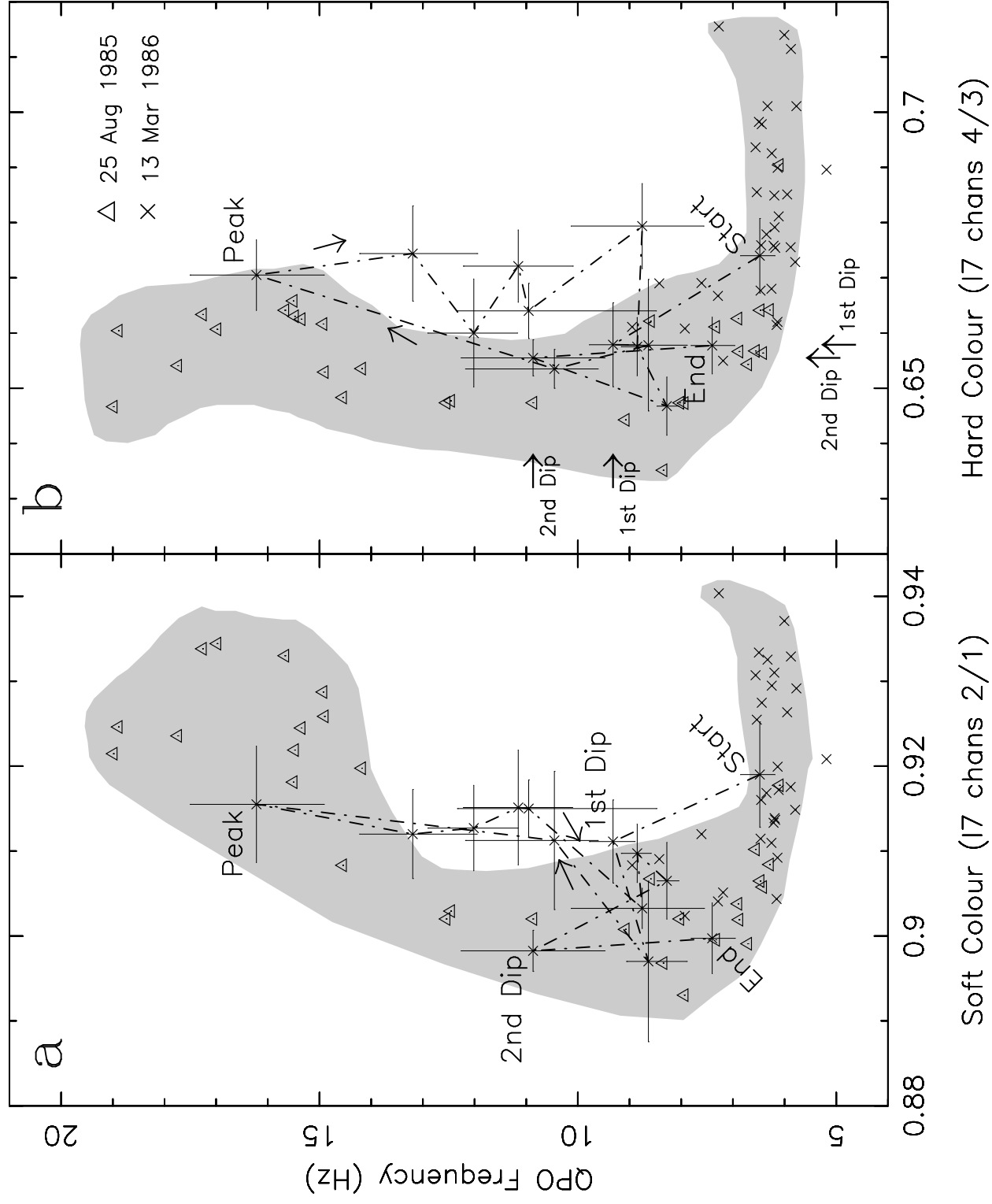


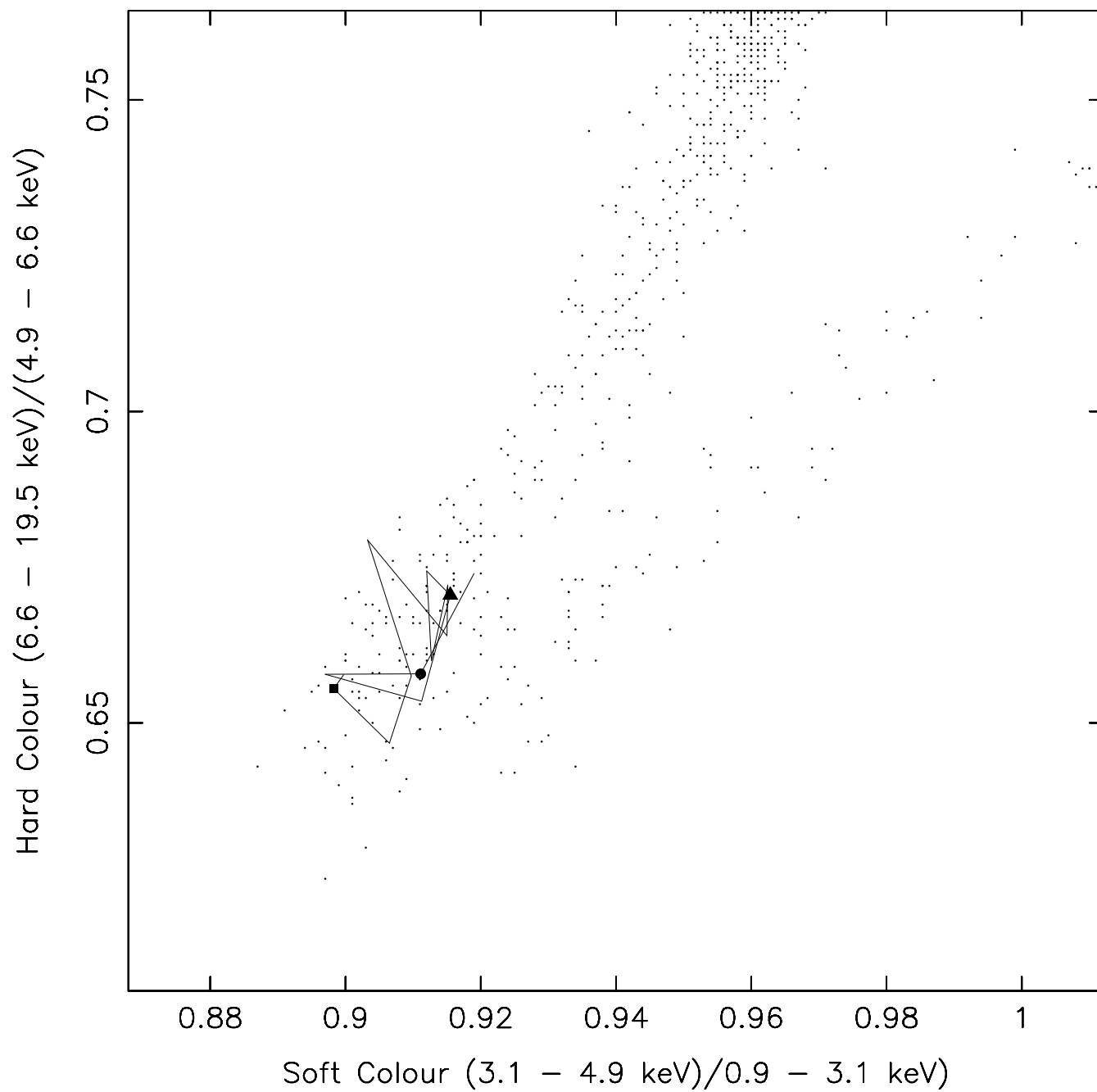


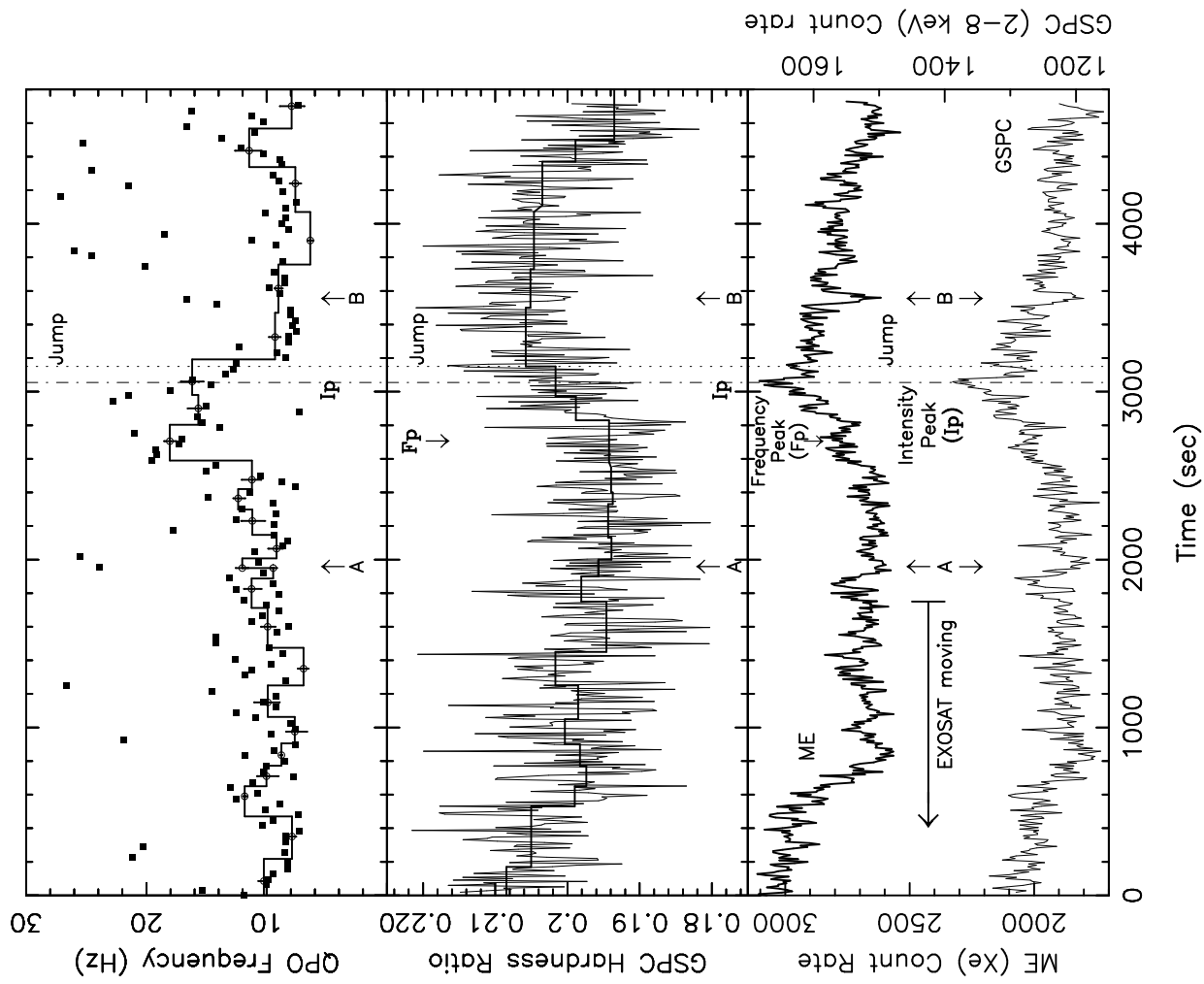


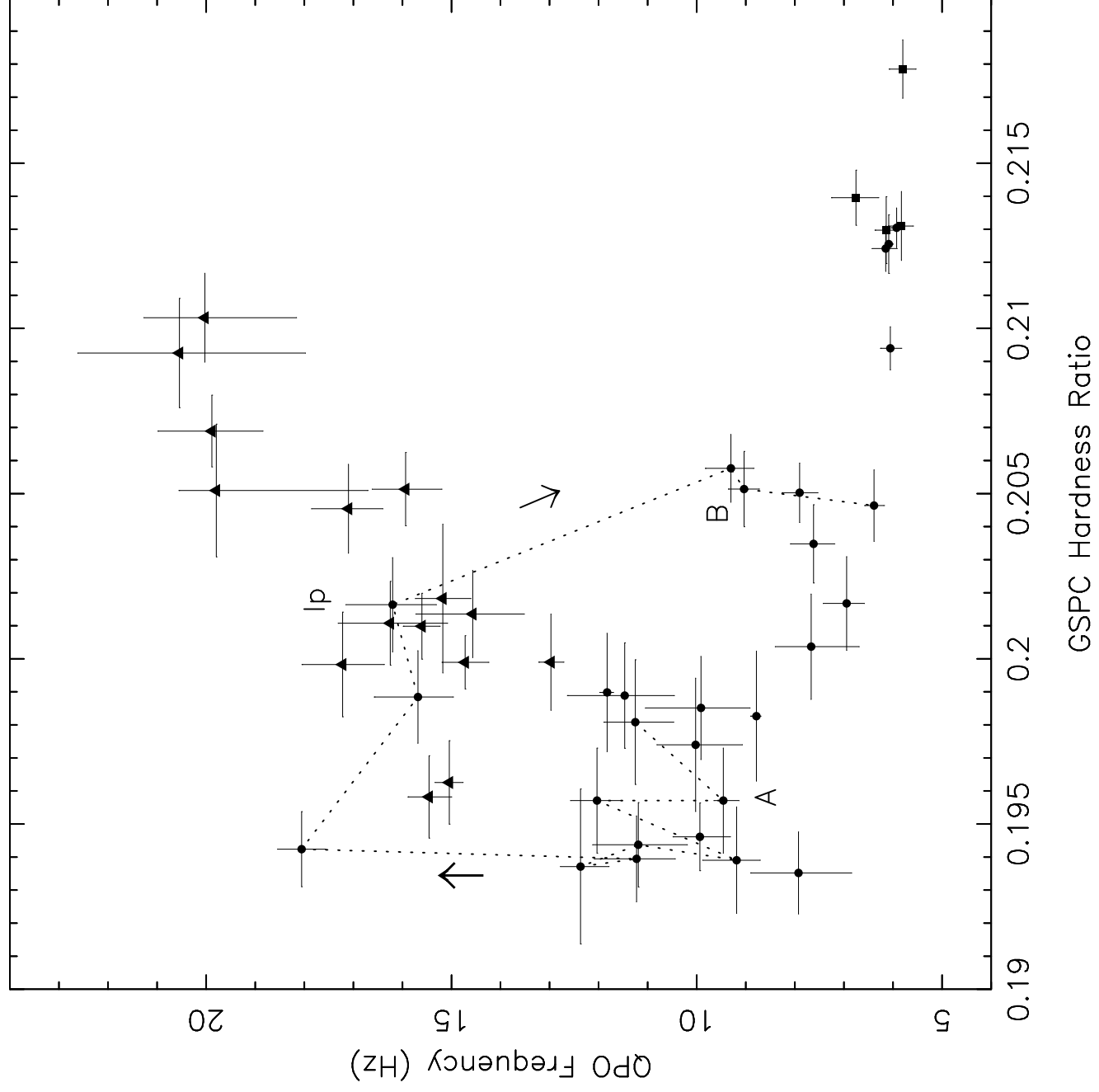


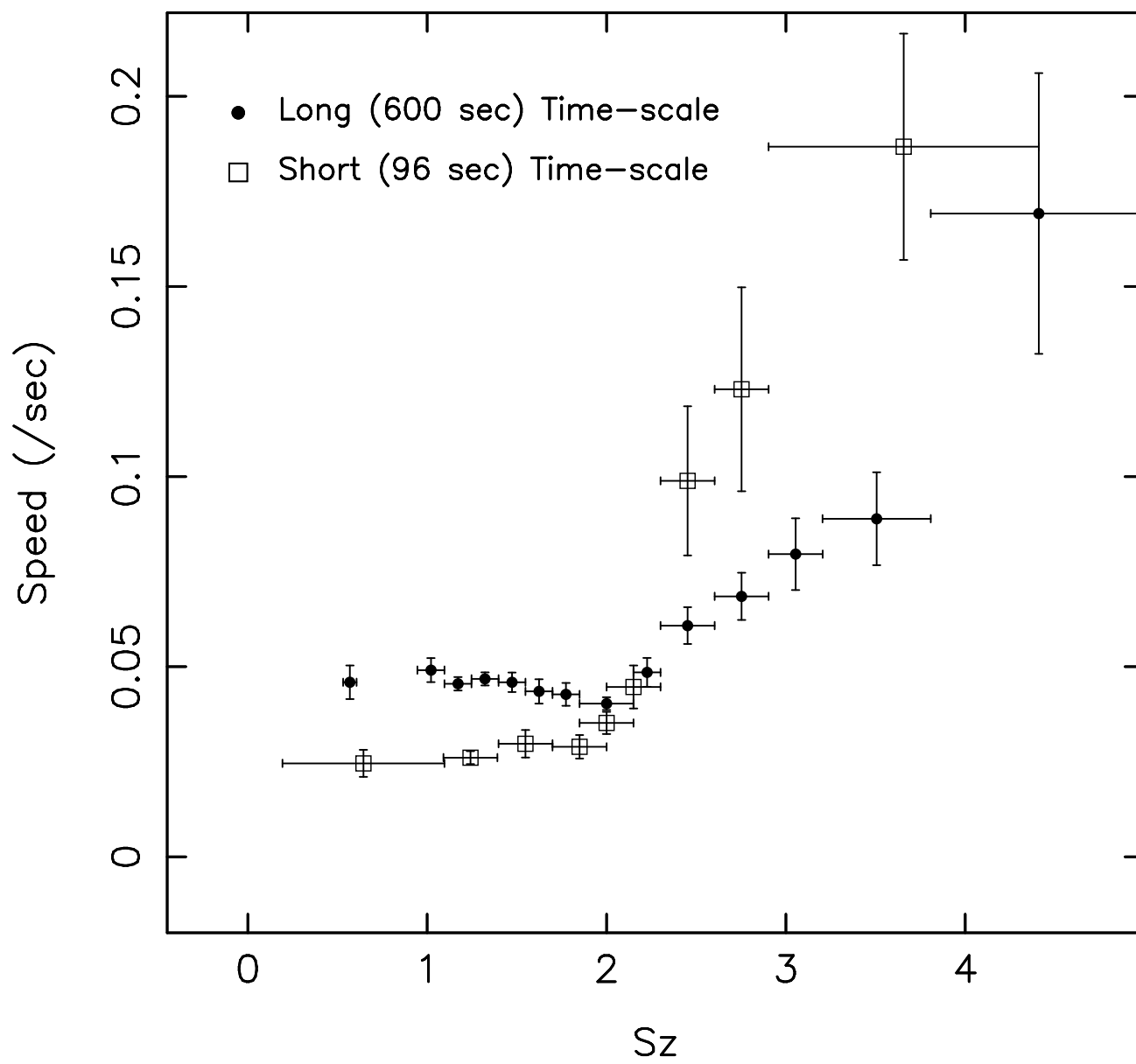












NORMAL BRANCH

FLARING BRANCH

